minerals

MDPI

Article

Mineralogical Constraints on the Pressure–Temperature Evolution of Granulites in the Bunger Hills, East Antarctica

Ilnur A. Abdrakhmanov [1], Yuri L. Gulbin [2,*], Sergey G. Skublov [2,3] and Olga L. Galankina [3]

[1] Gramberg Institute for Geology and Mineral Resources of the World Ocean (VNIIOkeangeologia), English Ave., 1, 190121 St. Petersburg, Russia; ilnur_01_95@mail.ru
[2] Department of Mineralogy, Crystallography, and Petrography, Saint-Petersburg Mining University (SPMU), 21 Line, 2, 199106 St. Petersburg, Russia; skublov@yandex.ru
[3] Institute of Precambrian Geology and Geochronology, Russian Academy of Sciences (IPGG RAS), Makarov Emb., 2, 199034 St. Petersburg, Russia
* Correspondence: ygulbin@yandex.ru

Abstract: Spinel- and orthopyroxene-bearing metapelitic granulites exposed in the Bunger Hills, East Antarctica, have been intensively studied in recent years because they are supposed to record evidence for UHT metamorphism. Detailed petrographic observations, as well as whole rock and mineral chemistry, together with SIMS trace element data on quartz, garnet, and orthopyroxene, are presented for these rocks. Mineral thermobarometry, including Al-in-orthopyroxene, ternary feldspar, Ti-in-quartz, and Fe-Ti oxide solvus, has been used to quantify the UHT conditions. Based on phase equilibrium modeling, a tight clockwise P-T path has been deduced, which involves near-isobaric heating at 6–7 kbar to ~950 °C followed by near-isobaric to slightly up-pressure cooling at 5–6 kbar to ~750 °C. It is concluded that the outlined metamorphic history is characteristic of an extensional crustal regime which is also evidenced by the correlation of prograde and retrograde metamorphism with the extensional and compressional phases of major ductile deformations recognized in the region. In order to constrain the tectonic setting of the granulites, this result is discussed in the context of current views on the Mesoproterozoic evolution of the Albany-Fraser Orogen, the westernmost part of which the Bunger Hills are considered to be.

Keywords: metapelitic granulite; spinel; orthopyroxene; garnet; mineral thermobarometry; isochemical phase diagram modeling; Theriak/Domino; REE mineral chemistry; UHT metamorphism; P-T path; Bunger Hills

check for updates

Citation: Abdrakhmanov, I.A.; Gulbin, Y.L.; Skublov, S.G.; Galankina, O.L. Mineralogical Constraints on the Pressure–Temperature Evolution of Granulites in the Bunger Hills, East Antarctica. *Minerals* **2024**, *14*, 488. https://doi.org/10.3390/min14050488

Academic Editor: Bernhard Schulz

Received: 7 March 2024
Revised: 18 April 2024
Accepted: 26 April 2024
Published: 4 May 2024

1. Introduction

Mineral assemblages of metamorphic rocks may be divided into prograde and retrograde ones. The prograde assemblages form when temperature and often pressure increase. The retrograde assemblages form either during rock cooling/decompression or later as a result of a discrete metamorphic event. Along with field relations and geochronology, mineral evidence (rock microstructures, mineral parageneses, mineral chemistry, zoning in minerals, etc.) gives an answer to a question concerning P-T path continuity or discontinuity which is very important for deciphering metamorphic history [1–9] (Hensen et al., 1995; Gibson, Wallmach, 1995; Jöns et al., 2006; Wiederkehr et al., 2008; Jeřábek et al., 2016; Liao et al., 2016; Zhou et al., 2019; Dwivedi et al., 2020; Huang et al., 2023).

In this article, we discuss the essential features of the metamorphic history of granulites in the Bunger Hills of East Antarctica deduced from petrography, mineral chemistry, and thermobarometry as well as phase equilibrium modeling. Many researchers consider the Bunger Hills to be a former westernmost part of the Albany–Fraser Orogen [10–12] (Sheraton et al., 1993; Clark et al., 2000; Morrissey et al., 2017), which was positioned along the southeastern margin of the Archaean Yilgarn Craton in Western Australia (Figure 1) and was formed in the late Mesoproterozoic during Rodinia assembly [13,14] (Smits et al., 2014;

Aitken et al., 2015). Granulite facies rocks exposed in the Bunger Hills are mainly tonalitic–granitic orthogneiss and garnet–sillimanite–cordierite (±spinel) paragneiss interlayered with felsic orthogneiss and mafic granulite. The igneous precursors of tonalitic–granitic orthogneiss were dated ca. 2800–2700 Ma [15] (Tucker et al., 2017) whereas those of felsic orthogneiss interlayered with metasedimentary rocks were dated ca. 1500–1700 Ma [16] (Sheraton et al., 1992). Zircon and monazite were from paragneiss record peak metamorphism at ca. 1220–1180 Ma, which coincides with Stage-2 of the Albany–Fraser Orogeny [17] (Tucker et al., 2018). These rocks document evidence that there was ultrahigh-temperature metamorphism with temperatures exceeding 900 °C [18,19] (Abdrakhmanov et al., 2021; Gulbin et al., 2022).

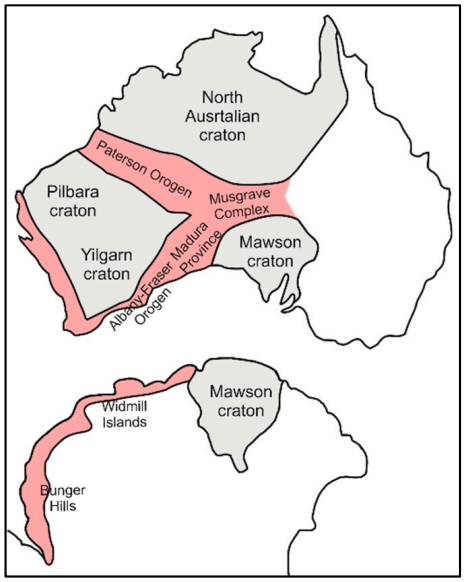

Figure 1. Location of the Bunger Hills with respect to the Yilgarn Craton and the Albany–Fraser Orogen.

There are different points of view on what is the type of P-T path of the granulites studied. In earlier works, an anticlockwise P-T evolution of the granulites in the Bunger Hills was thought possible [20] (Stüwe, Powell, 1989). The authors call attention to the fact that spinel in metapelitic assemblages is often overgrown by sillimanite, cordierite, and garnet. Hence, they concluded that compression with cooling occurred at the retrograde phase as a result of a post-peak event associated with crustal thickening due to the gravitational instability of the thinned lithosphere. This model assumes that the prograde history of the granulites was associated with crustal extension and decompression. Such a sequence is characteristic of extensional accretionary orogens (e.g., back-arc systems) where the thickening of the formerly extended crust accompanied by intense magmatic activity causes a near-isobaric cooling trajectory [21–25] (Harley, 1989; Collins, 2002a, 2002b; Brown, 2007; Kelsey, Hand, 2015).

As discussed later, the above-mentioned concept was questioned. Tucker and Hand (2016) and Tucker et al. (2018) use textural relationships between minerals of pelitic gneiss (partial replacement of garnet by cordierite). In [26] and [17], textural relationships between minerals of pelitic gneiss (partial replacement of garnet by cordierite) were used to conclude that peak granulite facies metamorphism in the Bunger Hills (800–960 °C, 5.5–7.1 kbar) and the adjacent Highjump Archipelago (850–950 °C, 6–9 kbar) was followed by decompression. Based on pseudosection modeling, they infer a clockwise P-T path with isobaric to slightly down-pressure cooling for metasedimentary rocks. According to the authors, this type of P-T path is also consistent with an extensional tectonic regime following arc accretion.

The aim of this article is as follows: (1) to present new data on the mineralogy and thermobarometry of metapelitic granulites in the Bunger Hills; (2) to detail the metamorphic processes at the prograde, peak, and retrograde phases of the P-T path; and (3) to use the

obtained results for a discussion of tectonic settings responsible for the late Mesoproterozoic metamorphism in the region.

2. Geological Setting

The Bunger Hills and northeastern Highjump Archipelago form the largest outcrops of Precambrian rocks in the Wilkes Land, East Antarctica. The geology of this area was studied by Soviet and Australian scientists [10,16,27–30] (Voronov, 1960; Ravich et al., 1968; Stüwe, Wilson, 1990; Sheraton et al., 1992, 1993, 1995). The Bunger Hills consist of massive felsic (orthopyroxene–quartz–feldspar) orthogneiss in the southeast and a layered gneiss series in the rest of the area (Figure 2). The layered series has a thickness of ca. 6–7 km and includes foliated and migmatized cordierite- and sillimanite-bearing gneiss (metapelitic granulites) (Figure 3a–g), garnet-bearing granitic gneiss, two-pyroxene and hornblende–pyroxene rocks (mafic granulites), minor garnet quartzite, calc–silicate rocks, and marble. These rocks are folded into a syncline which extends more than 25 km in a northwest direction and is modified by numerous tight, often isoclinal folds. Three systems of faults control the occurrence of mylonite and diaphthorite zones and divide the crystalline basement into separate blocks which have slightly moved relative to each other.

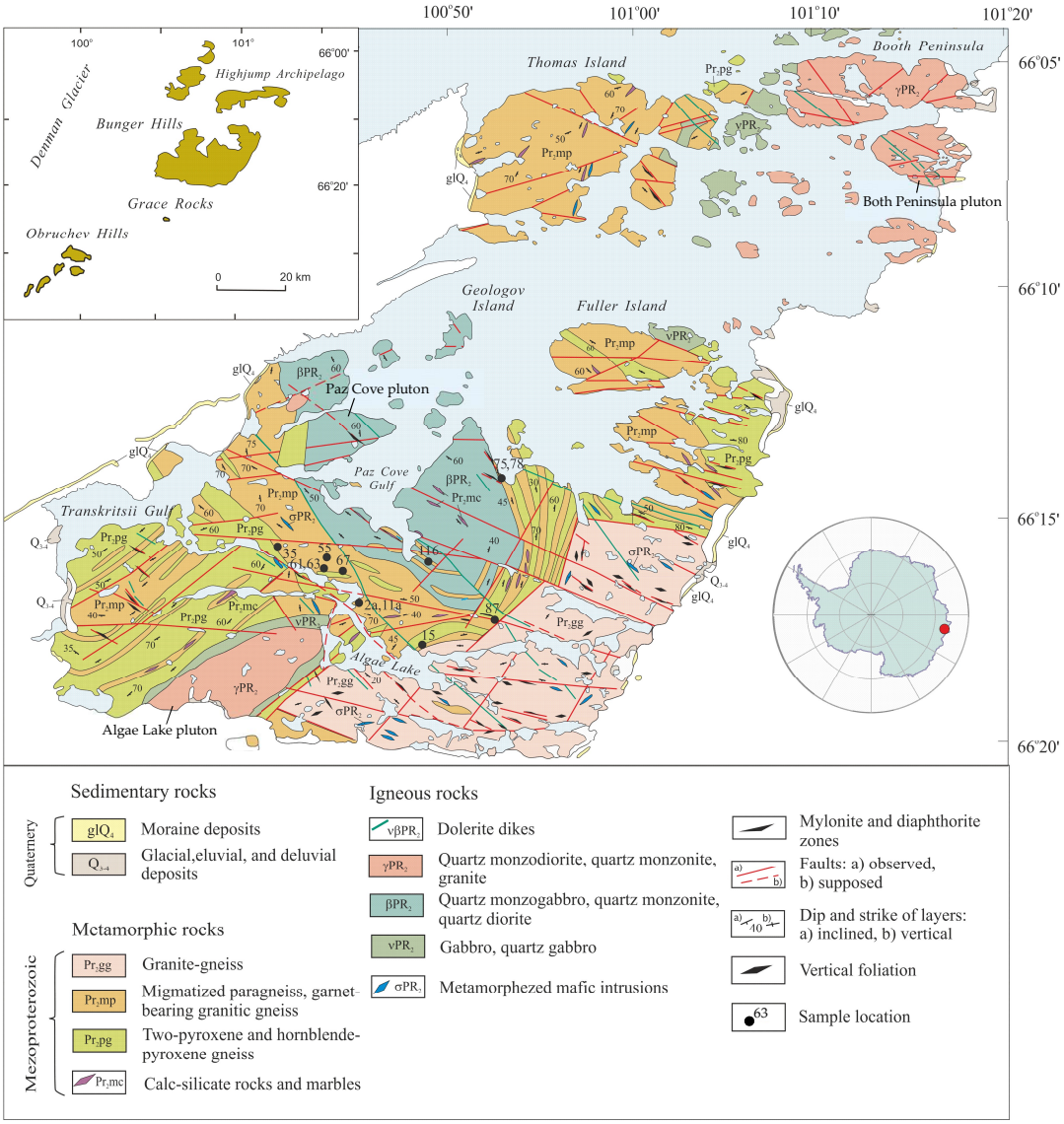

Figure 2. Geologic map of the Bunger Hills with the location of detailed study samples. From [28] Ravich et al. (1968).

Figure 3. Field photographs of outcrops of the layered gneiss series. (**a**) Typical appearance of foliated cordierite-bearing gneiss near the coastline of the Algae Lake; (**b**,**c**) appearance of migmatized sillimanite-bearing gneiss near the western end of the Paz Cove Gulf; (**d**–**g**) appearance of foliated paragneiss interlayered granite on the shore of the Ostrovnaya bay (eastern contact zone of the Paz Cove pluton). Location of sample 78; (**h**,**i**) appearances of folded paragneiss with bands of mafic granulite (black) and quartzite (white) intruded by pegmatite veins (rose) near the south shore of the Paz Cove Gulf.

The earliest pre-metamorphic magmatic event in the region is represented by metamorphosed mafic intrusions, up to a hundred meters thick and up to a few kilometers long, which are interlayered with paragneiss and felsic orthogneiss and are boudinaged everywhere. Syn-metamorphic igneous activity is evidenced by concordant and discordant granite and pegmatite veins, up to 4–5 m thick and up to a hundred meters long, whose composition is consistent with that of migmatitic leucosome (Figure 3h,i). Late- and post-metamorphic magmatism is recorded by three mafic to felsic plutons intruded in the layered gneiss series. Two of them (Algae Lake pluton and Paz Cove pluton) are placed in the southwestern and central Bunger Hills and consist of gabbroic rocks (gabbro, quartz gabbro, quartz monzogabbro, minor quartz monzonite, diorite, and quartz diorite). Another one (Booth Peninsula pluton) occurs in the east of the area studied and consists of charnockitic rocks (orthopyroxene-bearing granite, minor quartz monzodiorite, and quartz monzonite). According to [16] Sheraton et al. (1992), the gabbroic rocks formed at 1171 ± 3 Ma, whereas the charnockites crystallized at 1151 ± 5 Ma. According to [15] Tucker et al. (2017), enderbite from Paz Cove and Algae Lake plutons yields older ages (1200 ± 6 Ma and 1203 ± 3 Ma). Northwest-trending dikes of dolerite with an age of ca.

1140 Ma cut the country rocks and the plutons. The youngest igneous rocks in the area are alkaline mafic dykes emplaced at ca. 500 Ma.

Metapelitic granulites considered in this article are widespread in the Bunger Hills. Typical assemblages in these rocks are quartz–garnet–sillimanite, quartz–garnet–sillimanite–cordierite, quartz–garnet–cordierite, and quartz–garnet–cordierite–orthopyroxene (±sillimanite) [30] (Sheraton et al., 1995). Additionally, plagioclase, mesoperthitic K-feldspar, and biotite are present in these rocks as major minerals and hercynite spinel, gahnite, magnetite, ulvöspinel, corundum, ilmenite, and rutile are observed as accessory minerals. The listed oxides often form lamellar intergrowths produced by the breakdown of high-temperature solid solutions [18] (Abdrakhmanov et al., 2021).

3. Materials and Methods

This work is based on samples collected by one of the authors (I.A.A.) during the 64th Russian Antarctic Expedition of 2018/2019. Twelve samples were chosen for detailed petrographic and mineralogical studies. All of them are representative of the metapelitic granulites located in the central Bunger Hills (Figure 2).

Mineral textural relationships in these rocks were studied in thin sections under the Leica DM2700P polarizing microscope at the Saint-Petersburg Mining University. Bulk rock chemistry was determined by wet chemical analysis with UV-VIS spectrophotometry (UV-1650PC, Shimadzu Europe GmbH Germany) and atomic absorption spectrophotometry (AAS) with a flame atomizer (Quant-2, Kortek LLC, Russia and PFP7, Cole-Parmer, UK Jenway) at the VNIIOkeangeologia. Mineral compositions were analyzed using the JEOL JSM-7001F scanning electron microscope equipped with Oxford INCA Energy EDS system at the Saint-Petersburg Mining University and the JEOL JSM-6510LA electron microscope equipped with JED-2200 EDS at the IPGG RAS. Electron microprobe data are stored in the Supplementary Materials, which include representative analyses of minerals (Tables S1–S6) and back-scattered electron (BSE) images of the analyzed crystals as well as zoning profiles in garnet and orthopyroxene (Figures S1–S6).

Secondary ion mass spectrometry (SIMS) was used to measure trace element concentrations in quartz, garnet, and orthopyroxene. Measurements were performed with the Cameca IMS-4f ion microprobe at the Yaroslavl Branch of the Institute of Physics and Technology, Russian Academy of Sciences. The measurement technique is described by [31,32] Smirnov et al. (1995) and Nosova et al. (2002). All minerals were analyzed in situ, in thin sections for samples 15, 61, 63, 75, and 78, with a primary oxygen ion beam focused into a spot of ~20 µm. When constructing rare earth element (REE) patterns, REE contents were normalized to CI chondrite abundances [33] (McDonough, Sun 1995). The europium anomaly was calculated as $Eu/Eu^* = Eu_N/(Sm_N \times Gd_N)^{0.5}$.

In order to constrain the peak pressure and temperature of metamorphism and to derive the P-T paths, mineral thermobarometry based on the partitioning of major and trace elements between the minerals of the granulites was applied, including garnet–orthopyroxene [34,35] (Harley, Green, 1982; Lee, Ganguly, 1988), Ti-in-quartz [36,37] (Thomas et al., 2010; Huang, Audétat, 2012), Ti-in-biotite [38] (Henry et al., 2005), and re-integrated feldspar [39] (Hokada, 2001). Compositions of re-integrated feldspar were determined by two manners: (1) area scan SEM analysis and (2) the method proposed by [39] Hokada (2001), which included the computer image processing of back-scattered electron images with the ImageJ freeware tool (https://imagej.net/ij/ accessed on 25 April 2024) for an estimation of the area fractions of the host and lamellae domains in mesoperthitic/antiperthitic feldspar. In order to calculate temperatures with the two-feldspar geothermometer of [40] Fuhrman and Lindsley (1988), the GPT Excel spreadsheet [41] (Reche, Martinez 1996) was used.

Additionally, isochemical P-T equilibrium phase diagrams (pseudosections) were calculated using Theriak/Domino [42] (De Capitani, Petrakakis 2010) ver. 01.08.09 with the internally consistent thermodynamic database tcdb55c2d [43] (Holland, Powell 2004) and activity–composition relations for minerals occurring in granulites: feldspar [44] (Baldwin

et al., 2005), garnet, orthopyroxene, spinel, biotite, and liquid [45,46] (White et al., 2002, 2007), cordierite [43] (Holland, Powell 1998), sapphirine [47] (Kelsey et al., 2004), and ilmenite (ideal ternary solution of ilmenite, geikielite, and pyrophanite) for the MnO-Na_2O-CaO-K_2O-FeO-MgO-Al_2O_3-SiO_2-H_2O-TiO_2-O_2 (MnNCKFMASHTO) system. The bulk compositions used for phase equilibria modeling are provided in Table 1. Due to uncertainty in estimating H_2O contents, and because water has a great influence on phase diagram topologies, the H_2O activity was set as a calculation parameter to be estimated. In each sample, H_2O activity was selected in such a way that similarity was achieved between the calculated and observed mineral assemblages. Note that the a_{H2O} values thus obtained are not quantitative, but only indicate low or high water contents.

Table 1. Major element compositions (wt%) of the metapelitic granulites selected for this study.

Sample	2a	11a	15	35	55	61	63	67	75	78	87	116
Rock	GSC	GSC	GOC	GSC	GSC	GOC	GOC	GSC	GC	GC	GOC	GOC
SiO_2	70.22	64.18	70.62	52.94	55.99	48.57	68.77	65.83	65.51	61.13	68.82	69.82
TiO_2	1.03	0.92	0.54	2.43	1.22	1.12	0.52	0.68	1.06	1.00	0.56	0.36
Al_2O_3	12.89	16.39	12.43	19.19	17.98	23.69	14.28	15.34	15.12	16.46	12.30	14.95
Fe_2O_3	0.06	1.13	3.77	8.97	3.63	3.31	2.82	2.63	2.24	4.01	3.62	1.35
FeO	8.07	5.97	2.74	8.57	6.55	6.05	2.67	2.74	7.14	7.62	4.65	1.95
MnO	0.12	0.20	0.06	0.21	0.30	0.34	0.07	0.09	0.26	0.21	0.26	0.06
MgO	3.12	3.07	3.32	2.49	4.32	8.28	3.03	2.44	3.56	3.57	1.51	1.00
CaO	0.30	1.19	0.99	1.02	2.09	2.83	1.10	1.18	0.98	1.15	3.16	1.76
Na_2O	0.25	0.94	2.80	0.50	2.34	2.65	2.31	2.46	1.11	1.19	2.81	3.06
K_2O	1.75	3.82	1.63	2.49	3.89	2.11	3.33	5.61	1.41	2.07	1.45	5.17
P_2O_5	0.18	0.14	0.08	0.25	0.19	0.16	0.26	0.17	0.18	0.14	0.17	0.18
LOI	1.93	1.98	0.70	1.19	0.99	0.79	0.68	0.82	1.33	1.22	0.66	0.04
Total	99.93	99.94	99.69	100.24	99.49	99.91	99.83	100.00	99.90	99.79	99.96	99.69

Note: GSC, garnet–sillimanite (±cordierite) gneiss; GC, garnet–cordierite gneiss; GOC, garnet–orthopyroxene (±cordierite) gneiss.

Mineral abbreviations after [48] Whitney and Evans (2010).

4. Results

4.1. Petrography

4.1.1. Garnet–Sillimanite and Garnet–Sillimanite–Cordierite Gneiss (Samples 2a, 11a, 35, 55, 67)

These rocks contain garnet (10%–20% in cordierite-bearing gneiss, up to 50% in cordierite-free gneiss), sillimanite (commonly 6%–12%), cordierite (0%–20%), K-feldspar (mesoperthitic; 10%–30%), quartz (20%–30%), plagioclase (in places antiperthitic; 0%–15%), biotite (commonly 3%–5%), opaque minerals (magnetite + ilmenite; 3%–5%), and dark-green spinel (commonly 1%–3%). Accessory minerals include zircon, monazite, and corundum (up to 1%). Rutile (samples 2a, 11a, 35, 55; <1%) and graphite (sample 11a; up to 4%–5%) may also be present. The gneiss is characterized by a strong foliation defined by the interlayering of quartz–feldspar-rich domains with garnet–sillimanite (±cordierite) layers enriched with biotite, opaque minerals, and spinel.

The garnet occurs as relatively large (up to 2–3 mm) subhedral to euhedral crystals with polygonal and lobate morphologies (Figure 4a) containing inclusions of sillimanite, biotite, ilmenite, spinel, and rutile. Sillimanite forms three generations: (1) sillimanite I appears as fibrolite inclusions in garnet (Figure 4b); (2) sillimanite II corresponds to prismatic crystals up to 1 mm size, elongated along the foliation (Figure 4c). Sometimes prismatic sillimanite contains inclusions of spinel; (3) sillimanite III forms fine acicular crystals grown along the boundaries of cordierite grains and partially replacing this mineral (Figure 4d). Spinel is represented by two types: (1) spinel I forms inclusions in garnet, prismatic sillimanite, and cordierite; (2) spinel II is observed as isolated grains in garnet, sillimanite, and cordierite domains. Typically, spinel II and ilmenite overgrow on prismatic sillimanite and, moreover, spinel partially replaces sillimanite (Figure 4c). Also, both minerals occupy the interstitial

space between garnet grains and cordierite grains (Figure 4e,f). It is particularly remarkable that spinel II is a constituent of the quartz–feldspar matrix; therefore, direct contacts between spinel and quartz are observed. Biotite, except for small inclusions in garnet, occurs as larger crystals intergrown with garnet and forms aggregates of flakes which partially replace cordierite.

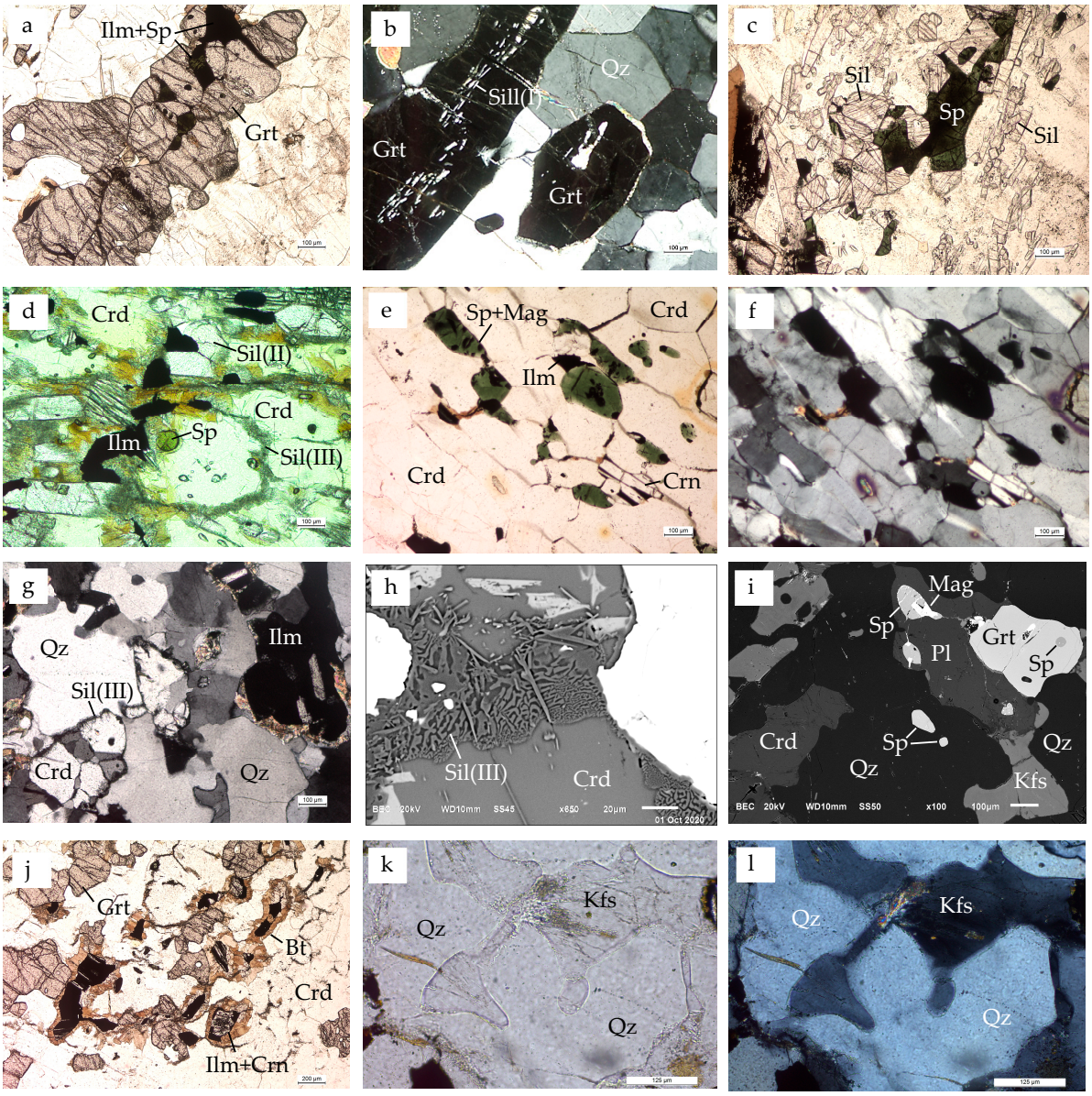

Figure 4. Mineral assemblages and textures of garnet–sillimanite–cordierite and garnet–cordierite gneiss. (**a**) Ilmenite and spinel located at the grain boundaries of garnet which also contain minute spinel inclusions. Sample 55; (**b**) fibrolitic sillimanite included within garnet. Sample 67; (**c**) prismatic sillimanite surrounded by ilmenite and spinel. Sample 55; (**d**) needle-like sillimanite grown together with biotite along grain boundaries of cordierite. Sample 2a; (**e**,**f**) ilmenite, spinel, and corundum occupying interstitial spaces between cordierite grains. Sample 67; (**g**) quartz–cordierite matrix. Cordierite grains are rimmed by fine needle-like sillimanite selvedges. Sample 78; (**h**) details of microstructure of the late-formed sillimanite aggregate. Sample 78; (**i**) inclusions of spinel in garnet and quartz. Sample 78; (**j**) ilmenite–corundum intergrowth separated from garnet and cordierite by biotite coronas. Sample 78; (**k**,**l**) quartz mantled by K-feldspar. Contours of the corona are emphasized by the Becke line. Microscope images in transmitted light (**a**,**c**–**e**,**j**,**k**), plane-polarized light; (**b**,**f**,**g**,**l**), cross-polarized light) and BSE images (**h**,**i**).

4.1.2. Garnet–Cordierite Gneiss (Samples 75, 78)

This variety of gneiss is composed of garnet (10%–20%), cordierite (25%–30%), quartz (20%–25%), K-feldspar (5%–20%), plagioclase (2%–20%), biotite (1%–3%), opaque minerals (magnetite + ilmenite; 4%–8%), spinel (1%–3%), and sillimanite (<1%). Accessory minerals are zircon, monazite, and corundum. It is texturally similar to previous rocks.

Cordierite is observed as a part of the quartz–feldspar matrix and forms lenticular aggregates of polygonal grains (0.2 to 0.4 mm) elongated along the foliation. Garnet occurs as elongated irregular grains including abundant inclusions of spinel and is in contact with cordierite. Sillimanite is represented only by the first and third generations (Figure 4g). Close inspection of late-formed sillimanite aggregates shows signs of a symplectitic microstructure (Figure 4h). Spinel forms euhedral grains up to 0.2 mm in size that are included within garnet, quartz (Figure 4i), feldspars, and cordierite. Spinel–ilmenite–magnetite (±corundum) intergrowths with exsolution textures are common (see details in [18] Abdrakhmanov et al., 2021). Spinel and opaque minerals may be mantled by cordierite, plagioclase, and biotite (Figure 4j). Coronas of K-feldspar around quartz are observed (Figure 4k,l) and indicate the partial melting of rocks [49] (Holness et al., 2011).

4.1.3. Garnet–Orthopyroxene (±Cordierite) Gneiss (Samples 15, 61, 63, 87, 116)

Major minerals are garnet (up to 25%–30%), orthopyroxene (up to 15%–20%), K-feldspar (mesoperthitic; commonly 15%–30%), plagioclase (locally antiperthitic; 0%–20%), quartz (25%–30%), cordierite (0%–20%), biotite (commonly 2%–7%, sometimes up to 15%–20%), opaque minerals (magnetite + ilmenite + ulvöspinel; 2%–6%), spinel (<1%), and sillimanite (<1%). Accessories are zircon, monazite, rutile, and corundum. The weakly manifested foliations are distinctive for these rocks.

Garnet and orthopyroxene are hosted within the quartz–feldspar (±cordierite) matrix and occur as irregular to euhedral grains of 1–3 mm in size (Figure 5a). Both minerals are often intergrown with each other and with biotite. In so doing, the garnet is generally overgrown and partially replaced by orthopyroxene (Figure 5b). Inclusions of orthopyroxene in the garnet are also found (Figure 5c). The garnet also includes biotite, fibrolitic sillimanite, spinel, and ilmenite (Figure 5c,g). The same minerals are observed in the matrix where they are concentrated in the interstitial spaces between grains. Orthopyroxene contains thin exsolution lamellae. In many cases, it is partly consumed by mica-like mineral (Figure 5b,d) or replaced by symplectitic intergrowths of biotite and quartz (Figure 5b,f). K-feldspar and plagioclase occur as smaller homogeneous grains and larger heterogeneous ones with exsolution textures (mesoperthitic and antiperthitic). Typically, exsolution lamellae are placed in the core of the grains and mantled by homogeneous outer domains (Figure 5h,i).

4.2. Mineral Chemistry

4.2.1. Major Elements

A summary of the mineral compositions from the studied samples is given in the Supplementary Materials. The major features of the mineral chemistry are presented below.

Garnet–Sillimanite and Garnet–Sillimanite–Cordierite Gneiss

The garnet is weakly zoned pyrope-rich ($X_{Py} = Fe/(Fe + Mg + Mn + Ca)$, varies from 0.31 to 0.39 in different samples), spessartine- and grossular-poor ($X_{Sps} = Mn/(Fe + Mg + Mn + Ca) < 0.07$, $X_{Ca} = Ca/(Fe + Mg + Mn + Ca) < 0.05$) almandine. Occasionally, when garnet intergrows with cordierite and biotite, the garnet rims show lower values of X_{Py} (up to 0.23–0.25) reflecting retrograde Mg-Fe exchange (Table S1, Figure S1).

The cordierite is magnesian ($X_{Mg} = Fe/(Fe + Mg)$ 0.78–0.85) and has low totals (~93–97 wt%) indicating the presence of volatiles in its structural channels (Table S2).

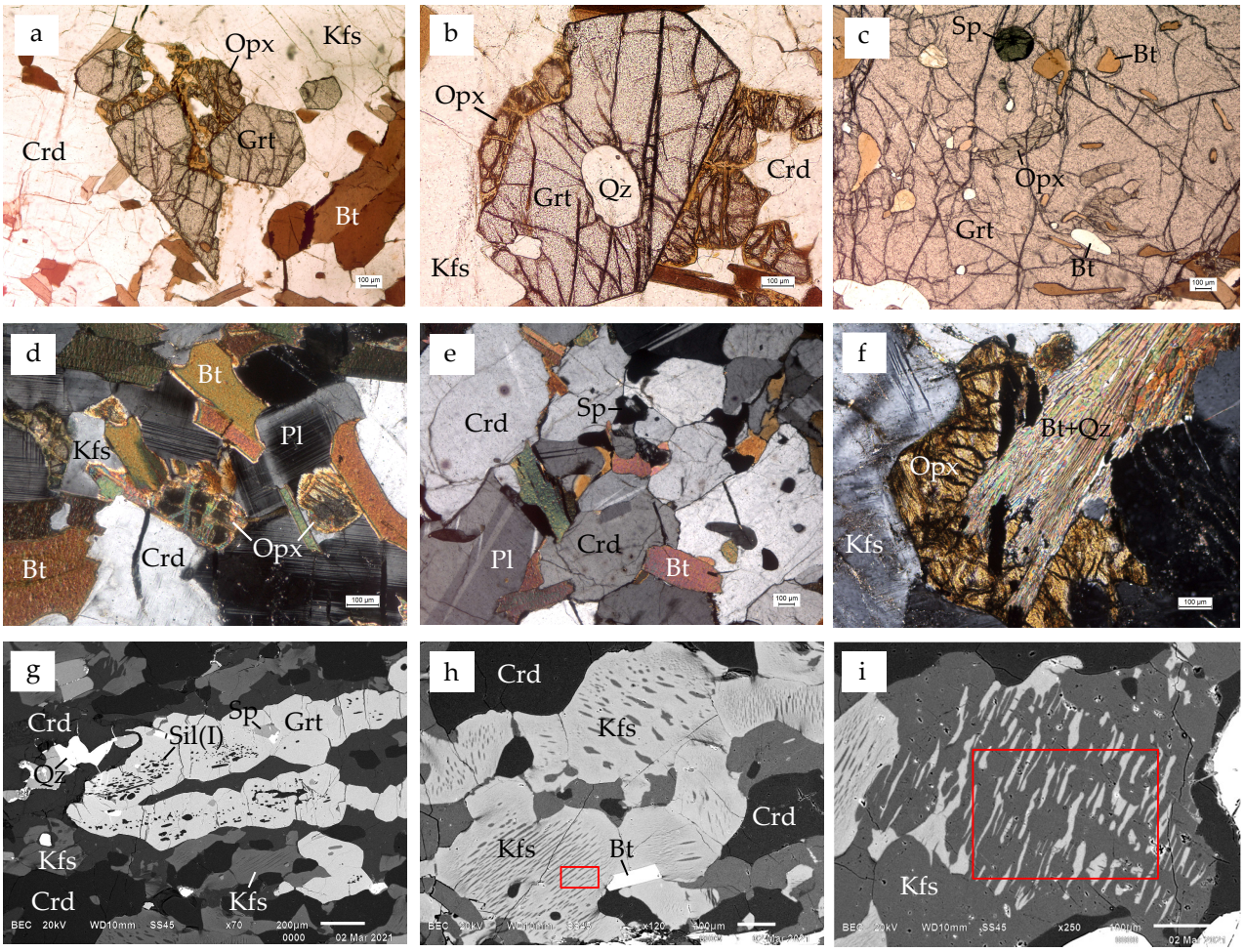

Figure 5. Mineral assemblages and textures of garnet–orthopyroxene (±cordierite) gneiss. (**a**) Garnet and orthopyroxene hosted within the feldspar–cordierite matrix. Sample 61; (**b**) garnet overgrown by orthopyroxene. Sample 61; (**c**) inclusions of orthopyroxene, spinel, and biotite in garnet. Sample 61; (**d**) altered orthopyroxene in the feldspar–cordierite matrix. Sample 61; (**e**) spinel located in the interstitial spaces between cordierite and plagioclase grains. Sample 61; (**f**) orthopyroxene partially replaced by quartz–biotite symplectitic intergrowths. Sample 15; (**g**) elongate garnet with inclusions of quartz and sillimanite in the quartz–feldspar matrix. Sample 63; (**h**,**i**) mesoperthitic K-feldspar and antiperthitic plagioclase. Sample 63. Area scan SEM analyses are outlined in red. Microscope images in transmitted light (**a**–**c**, plane-polarized light; **d**–**f**, cross-polarized light) and BSE images (**g**–**i**).

The biotite corresponds to phlogopite (Mg# = Mg/(Mg + Fe) 0.65–0.85) and varies in composition according to its microstructural position (Table S3, Figure S2). The biotite included in the garnet is more magnesian than the biotite in the matrix. This is particularly true for samples 2a, 11a, and 55, where both types of biotite have Mg# values between 0.78 and 0.65–0.70, between 0.84–0.85 and 0.72–0.75, and between 0.78–0.79 and 0.73–0.77, respectively. The TiO_2 content in these types of biotite mostly ranges between 3.3 and 4.9 wt%, rising to 6 wt%. Late-stage fine-flaked biotite occurring in sample 2a has a lower TiO_2 (0.3–3.0 wt%) but a higher Mg# (up to 0.85). A tendency of increasing Mg# values in late-stage biotite agrees with the enrichment in magnesium content from the core (Mg# 0.75) to rim (Mg# 0.80) of the biotite plate replacing the garnet rim (Figure S2c).

The K-feldspar is orthoclase-rich ($X_{Ort} = K/(Ca + Na + K)$ 0.84–0.94) and anorthite-poor ($X_{An} = Ca/(Ca + Na + K) < 0.01$) with low BaO content (<1.6 wt%). Often, the K-feldspar grains contain a great fraction of the perthitic exsolution lamellae of albite ($X_{Ab} = Na/(Ca + Na + K)$ 0.92–1.00) (Table S4). In sample 2a, mesoperthite is most abundant and has re-integrated (pre-exsolution) compositions of Na-rich feldspar with

X_{Ab} values between 0.63 and 0.67 and X_{Ort} values between 0.37 and 0.33. The absence of anorthite in the feldspar is caused by the low bulk-rock CaO content (0.30 wt%). The same reason explains the absence of plagioclase in the mineral assemblage of sample 2a. In other samples, plagioclase is characteristic and has compositions of oligoclase–andesine with X_{An} of 0.26–0.38 (samples 35, 55, 67) and andesine–labrador with X_{An} of 0.43–0.52 (sample 11a). Sometimes, plagioclase grains contain antiperthitic exsolution lamellae of K-feldspar with X_{Ort} of 0.90–0.93 and X_{Ab} of 0.10–0.07 (Table S4, Figure S3c).

The spinel is hercynite with minor ZnO and Cr_2O_3. The Fe^{3+} content is low (<0.80 apfu). The ZnO amount is variable, which leads to the presence of Zn-poor and Zn-rich spinel (Table S5, Figure S4). Zn-poor spinel occurs in samples 55 and 67. In these samples, $X_{Hc} = Fe^{2+}/\left(Fe^{2+} + Mg + Zn\right)$ ranges between 0.56 and 0.62, ZnO varies between 1.3 and 3.1 wt%, and Cr_2O_3 varies between 0.2 and 1.7 wt%. Zn-rich spinel occurs in samples 2a and 11a. In these samples, X_{Hc} ranges between 0.50 and 0.56, ZnO varies between 7.2 and 8.2 wt% (sample 2a) and between 11.4 and 13.9 wt% (sample 11a), and Cr_2O_3 varies between 2.1 and 3.4 wt%.

The ilmenite in all samples has minor MgO (<0.8 wt%) and MnO (<0.5 wt%). In samples 2a, 11a, and 55, the ilmenite has low hematite content with $X_{Hem} = Fe^{3+}/2$ no more than 0.03. In sample 67, where banded magnetite–ilmenite intergrowths are widely developed and the ilmenite contains fine hematite exsolution lamellae, X_{Hem} values are higher, ranging between 0.08 and 0.13. Magnetite is found in samples 55 and 67 and has minor V_2O_5 (<0.8 wt%).

Garnet–Cordierite Gneiss

The garnet is weakly zoned pyrope-rich (X_{Py} 0.29–0.31) almandine showing depletion in Mn (X_{Sps} < 0.05) and Ca (X_{Grs} < 0.03) (Figure S1b). The cordierite is magnesian with X_{Mg} values between 0.80 and 0.85.

The biotite is Ti-rich phlogopite with a composition depending on its microstructural position. The biotite included in the garnet has more Mg# (0.73–0.75) and TiO_2 (4.5–4.7) compared to the biotite in the matrix (Mg# 0.67–69, TiO_2 3.2–3.6 wt). The biotite-mantled intergrowths of spinel and opaque minerals are relatively Mg-rich (Mg# 0.69–0.73) and Ti-poor (TiO_2 3.0–3.3). The late-stage biotite replacing cordierite grown along grain boundaries is slightly Mg-poor (Mg# 0.67–0.68) and Ti-poor (TiO_2 3.1–3.3) (Figure S2f,g).

The K-feldspar is orthoclase-rich (X_{Ort} 0.85–0.90) and anorthite-poor (X_{An} < 0.01) with low BaO content (<1.3 wt%). The plagioclase has compositions of oligoclase–andesine with X_{An} of 0.24–0.36 no matter whether it occurs in the matrix as individuals or mantles the spinel–magnetite–ilmenite intergrowths (Figure S3d).

The spinel is Zn-poor and Zn-rich hercynite with small amounts of Cr_2O_3 (0.2–1.2 wt%, occasionally up to 2.2 wt%) and MnO (<0.4 wt%). The Fe^{3+} content is low (<0.70 apfu). In sample 75, Zn-poor spinel with ZnO of 0.6–2.2 wt% is the dominant phase. At this point, the spinel included in the garnet is Mg-poor (X_{Hc} 0.53–0.57) compared to the spinel in the matrix (X_{Hc} 0.61–0.72). In sample 78, Zn-poor spinel (ZnO 2.0–3.1 wt%, X_{Hc} 0.55–0.59) occurs as inclusions in the garnet, whereas Zn-rich spinel (ZnO 10–17 wt%, $X_{Ghn} = Zn/(Fe^{2+} + Mg + Zn$ 0.20–0.34, X_{Hc} 0.38–0.52) is found in the matrix (Table S5). It is possible that Zn-rich spinel appeared as a result of diffusion processes promoted by the partial replacement of spinel by magnetite (Figure S4e,f).

The ilmenite has low MgO (<0.9 wt%) and MnO (<0.4 wt%). In sample 75, where magnetite–ilmenite intergrowths are found, X_{Hem} is no more than 0.02. In samples 78, where such intergrowths also occur, X_{Hem} occasionally increases to 0.08–0.10. Magnetite has minor V_2O_5 (0.3–1.2 wt%).

Garnet–Orthopyroxene–Cordierite Gneiss

The garnet is weakly zoned almandine with minor spessartine (X_{Sps} < 0.05) and grossular (X_{Ca} < 0.03) components. X_{Py} ranges between 0.31 and 0.33 in samples 87 and 116, between 0.34 and 0.35 in sample 15, and between 0.38 and 0.40 in samples 61 and 63.

The garnet rims adjacent to cordierite and biotite exhibit lower values of X_{Py} (up to 0.21 in sample 15 and up to 0.31–0.32 in samples 61 and 63) due to the retrograde exchange of Fe and Mg (Figure S1c–e).

The orthopyroxene is enstatite with high aluminum content. In sample 15, $X_{En} = Mg/(Fe + Mg)$ ranges between 0.57 and 0.58, Al_2O_3 between 6.8 and 9.0 wt%, and $X_{Al}^{M1} = Si - (2 - Al)$ between 0.13 and 0.18. In sample 61, X_{En} ranges between 0.62 and 0.65, Al_2O_3 between 6.4 and 8.2 wt%, and X_{Al}^{M1} between 0.15 and 0.18. In sample 63, X_{En} ranges between 0.58 and 0.61, Al_2O_3 between 7.3 and 9.2 wt%, and X_{Al}^{M1} between 0.15 and 0.19. In sample 116, X_{En} ranges between 0.55 and 0.56, Al_2O_3 between 5.6 and 6.1 wt%, and X_{Al}^{M1} between 0.06 and 0.07. The orthopyroxene in samples 15 and 61 shows weak core-to-rim zoning with cores enriched in aluminum (sample 15: Al_2O_3 7.8–8.2 wt%, X_{Al}^{M1} 0.17; sample 61: Al_2O_3 8.0, X_{Al}^{M1} 0.18) relative to the rims (sample 15: 6.8–7.2 wt%,%, X_{Al}^{M1} 0.15; sample 61: Al_2O_3 7.5, X_{Al}^{M1} 0.15) (Table S1, Figure S1d,f).

The cordierite has X_{Mg} values between 0.82 and 0.88. The biotite in the matrix of all samples is phlogopite with Mg# values ranging between 0.64 and 0.73, and TiO_2 content between 3.6 and 5.1 wt%. Rare biotite included in the garnet shows higher Mg# (0.80) and TiO_2 (up to 5.5 wt%)

K-feldspar and plagioclase occur in samples 87 and 116. The K-feldspar is orthoclase-rich (X_{Ort} 0.84–0.92) and anorthite-poor (X_{An} < 0.01) with low BaO content (<1.1 wt%). The plagioclase corresponds to oligoclase–andesine with X_{An} of 0.26–0.32. In addition to homogeneous feldspars, mesoperthite and antiperthite are common in the gneiss. In samples 15, mesoperthite is an intimate intergrowth of albite (X_{Ab} 0.92–0.93, X_{An} 0.07–0.06, X_{Ort} 0.01) and K-rich feldspar (X_{Ort} 0.58–60, X_{Ab} 0.37–0.36, X_{An}0.05–0.04) (Figure S3e,f). The re-integrated composition is Na-rich feldspar (X_{Ab} 0.74–0.79, X_{Ort} 0.20–0.14, X_{An} 0.06–0.07). In sample 63, the host composition of mesoperthitic K-feldspar (X_{Ort} 0.86–0.87, X_{Ab} 0.14–0.13) is the same as the lamellae composition of antiperthitic plagioclase feldspar (X_{Ort} 0.85, X_{Ab} 0.15). Much of the same is true for the host in antiperthitic plagioclase (X_{Ab} 0.78, X_{An} 0.22) and the lamellae in mesoperthitic K-feldspar (X_{Ab} 0.78–0.77, X_{An} 0.20–0.22, X_{Ort} 0.02–0.01). Re-integrated compositions, calculated for mesoperthitic and antiperthitic ternary feldspar with the [39] Hokada (2001) method, correspond to K-rich feldspar (X_{Ort} 0.60, X_{Ab} 0.33, X_{An} 0.07) and Na-rich feldspar (X_{Ab} 0.64, X_{Ort} 0.19, X_{An} 0.17).

Spinel is found in samples 61 and 63. The spinel is Zn-poor and Cr-poor hercynite. In sample 61, ZnO and Cr_2O_3 contents range between 1.5 and 2.7 wt% and between 0.5 and 1.5 wt%, respectively. In sample 63, ZnO contents mainly range between 1.9 and 3.0 wt%, occasionally rising to 5.0–5.3 wt%, and Cr_2O_3 contents vary between 0.0 and 0.4 wt%. In both samples, the spinel included in the garnet shows lower Mg# values (0.47 in sample 61, 0.44–0.49 in sample 63) than that in the matrix (0.53–0.58 in sample 61, 0.52–0.60 in sample 63).

The ilmenite is low in MgO (<1.6 wt%) and MnO (<0.8 wt%). X_{Hem} mostly varies between 0.02 and 0.10. The magnetite has minor V_2O_5 (0.0–1.0 wt%). Titaniferous magnetite is found only in sample 63. The titaniferous magnetite is rich in the ulvöspinel component with X_{Ulv} = Ti values ranging from 0.38 to 0.78. The ilmenite associated with titaniferous magnetite shows the highest X_{Hem} values (up to 0.24) (Table S6). They are regarded as products of exsolution and are closely associated with corundum and acicular rutile [18] (Abdrakhmanov et al., 2021).

4.2.2. Trace Elements

A summary of trace element mineral compositions is given in Tables 2 and 3.

According to SIMS analysis, the quartz in the granulites studied is enriched in Ti. The highest content of this element was determined in the garnet–cordierite gneiss (sample 75, up to 245–280 ppm; sample 78, up to 220–245 ppm). In the quartz from sample 63, the concentration of Ti is lower (108–172 ppm).

In sample 15, the garnet is unzoned from core to rim and exhibits overall enrichment in middle and heavy rare earth elements (M-HREE) relative to the other samples (Gd_N

360–390, Yb_N 900–1170); it shows a slightly positive M-HREE slope (Yb_N/Gd_N 2.3–3.2) and a strong negative Eu anomaly (Eu/Eu* 0.02–0.04) (Figure 6, sample 15). In addition to REE, the garnet displays strong enrichment in Y (1300–1650 ppm) and Hf (68–81 ppm). The orthopyroxene in the same sample is also enriched in M-HREE (Gd_N 11–16, Yb_N 7–9) and additionally in Ti (1020–7670 ppm). It shows a flat to slightly negative M-HREE slope (Yb_N/Gd_N 0.4–0.9) and a strong negative Eu anomaly (Eu/Eu* 0.02). The values of the orthopyroxene/garnet M-HREE distribution coefficients, D_{HREE}(Opx/Grt), are close to equilibrium values 0.01–0.03 [50] (Harley, Kelly 2007) and decrease monotonically from Gd (0.03–0.04) to Yb (0.008–0.01).

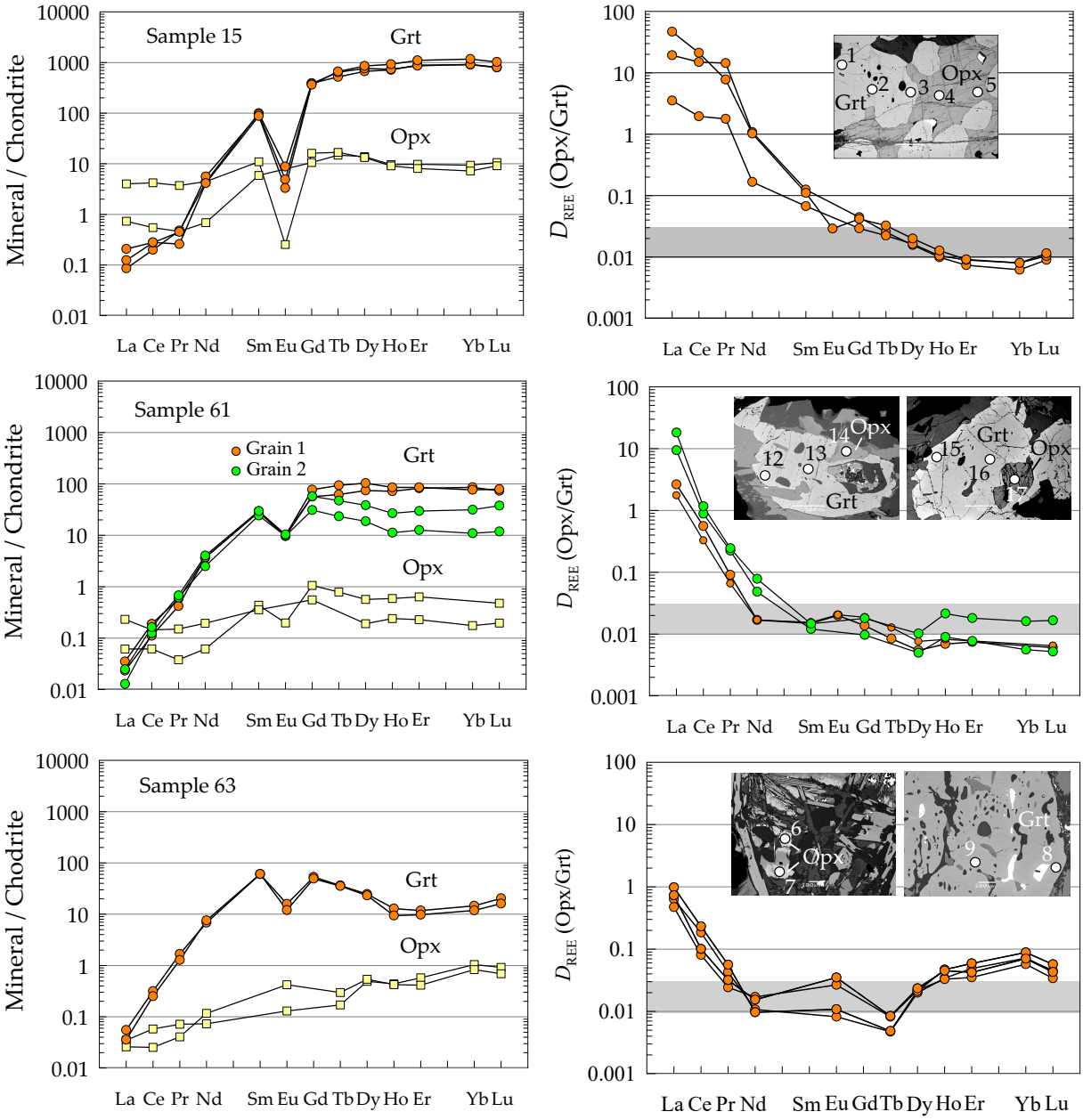

Figure 6. Chondrite normalized REE for minerals from sample 15, 61, and 63 (**left**) and their associated orthopyroxene–garnet partitioning profiles (**right**). The gray area represents the equilibrium values of D_{HREE}(Opx/Grt) from [50] Harley and Kelly (2007). BSE images show the studied crystals with points of analysis (see details in Figure S6).

In sample 61, two garnet grains were studied (Figure 6, sample 61). The grain 1 is unzoned with higher M–HREE contents (Gd_N 56–77, Yb_N 76–86) and a flat M-HREE

slope (Yb_N/Gd_N 0.4–1.5). In the grain 2, M-HREE contents are lower and decrease from the core (Gd_N 57, Yb_N 31) to the rim (Gd_N 31, Yb_N 11). The M-HREE pattern for this grain has a break near Ho (YbN/Ho_N 1.0–1.2). Also, the grains differ noticeably in their contents of Y (grain 1: 116–139 ppm; grain 2: 23–45 ppm) and Hf (grain 1: 7–8 ppm, grain 2: 3–4 ppm). REE patterns yield a negative Eu anomaly (Eu/Eu* 0.21–0.36) in both cases. The orthopyroxene in the same sample is depleted in M-HREE (Gd_N 0.5–1.0, Yb_N 0.18–0.21) and Ti (590–800 ppm). It shows a slightly negative M-HREE slope (Yb_N/Gd_N 0.2–0.7) and a negative Eu anomaly (Eu/Eu* 0.29). The values of D_{HREE}(Opx/Grt) are close to equilibrium in the case of Gd (0.01–0.02) and Tb (0.008–0.012) and below equilibrium in a row of Dy-Lu (0.005–0.008). The exception is provided by the orthopyroxene–garnet partitioning profile for the rim of garnet (grain 2) which exhibits equilibrium values of D_{HREE}(Opx/Grt) for all M-HREE (0.010–0.018).

Table 2. Trace element concentrations (ppm) in quartz from the granulites studied and the results of thermobarometry calculations.

Sample	**15**	**15**	**63**	**63**	**75**	**75**	**75**	**78**	**78**	**78**	**78**
Analysis	**1**	**2**	**10**	**11**	**18**	**19**	**20**	**1**	**2**	**3**	**4**
Li	0.09	0.07	0.24	0.74	0.04	0.07	0.09	0.40	0.12	0.03	0.04
Na	10.1	10.4	132	1460	104	131	259	8.42	7.60	4.54	15.9
Al	88.0	61.4	131	140	177	132	125	23.7	22.9	33.4	78.9
K	9.44	7.80	70.5	957	143	296	307	20.0	26.7	21.0	62.2
Ti	165	154	108	173	264	280	245	244	221	155	223
Mn	0.33	0.24	0.43	1.32	2.65	1.78	1.79	0.55	0.63	0.69	1.25
Fe	76.6	36.4	114	1467	609	1257	439	57.0	65.6	64.4	162.7
Rb	0.04	0.04	1.15	1.87	0.49	0.99	0.92	0.25	0.30	0.23	0.26
Sr	0.05	0.02	1.10	0.57	0.21	0.50	0.61	0.20	0.23	0.19	0.19
Ba	0.05	0.02	0.24	0.73	0.36	0.98	1.01	0.14	0.52	0.23	0.17
T_{T10}, °C	720–745	710–735	670–695	725–750	775–800	785–810	765–790	765–790	755–780	710–735	755–780
T_{HA12}, °C	905–925	895–910	845–860	910–930	975–1000	985–1010	965–985	965–985	950–970	895–915	950–970

Note: T_{T10}, temperature estimated with Thomas et al. (2010) geothermometer [36]; T_{HA12}, with Huang and Audétat (2012) geothermometer [37] for P = 6–7 kbar.

Table 3. Trace element concentrations (ppm) in garnet and orthopyroxene from the granulites studied.

Sample	**15**	**15**	**15**	**15**	**15**	**61**	**61**	**61**
Mineral	**Grt**	**Grt**	**Grt**	**Opx**	**Opx**	**Grt ***	**Grt ***	**Opx ***
Analysis	**1(r)**	**2(c)**	**3(r)**	**4**	**5**	**12(r)**	**13(c)**	**14**
Ti	140	136	112	7676	1020	205	227	803
V	55.1	63.6	59.6	136	113	83.7	83.5	245
Y	1036	1410	1652	17.2	15.9	116	139	0.76
Zr	40.6	20.2	15.0	6.95	7.58	45.2	45.5	5.41
Nb	0.06	0.04	0.03	16.8	0.11	0.070	0.044	0.045
Hf	68.5	72.2	81.5	1.98	1.91	6.99	8.34	0.566
La	0.02	0.03	0.05	0.17	0.95	0.008	0.005	0.015
Ce	0.12	0.17	0.17	0.34	2.58	0.115	0.068	0.038
Pr	0.04	0.04	0.02	0.04	0.34	0.053	0.038	<0.005
Nd	1.99	2.55	1.88	0.31	2.03	1.67	1.67	0.028
Sm	14.7	14.0	13.0	0.87	1.62	4.17	4.35	0.064
Eu	0.49	0.28	0.19		0.14	0.542	0.555	0.011
Gd	77.4	76.2	72.3	2.11	3.21	11.2	15.3	0.210
Tb	18.7	23.2	24.0	0.53	0.61	2.24	3.40	0.028
Dy	164	188	209	3.41	3.27	18.3	25.5	0.139
Ho	39.1	40.2	50	0.52	0.50	3.93	4.67	0.032
Er	142	138	176	1.56	1.30	13.1	13.6	0.102
Y	146	148	188	1.50	1.16	13.9	12.3	0.034
Lu	19.6	19.8	25.1	0.26	0.22	1.80	1.93	0.012

Table 3. *Cont.*

Sample	61	61	61	63	63	63	63
Mineral	Grt **	Grt **	Opx **	Grt	Grt	Opx	Opx
Analysis	15(r)	16(c)	17	8(r)	9(c)	6	7
Ti	138	208	594	159	168	588	807
V	77	85	238	67	81	374	413
Y	23	45	0.209	21	19	0.624	0.660
Zr	22	43	2.91	26	45	5.0	6.0
Nb	0.029	0.024	0.067	0.118	0.032	0.127	0.229
Hf	1.92	3.67	0.286	3.1	2.7	0.780	1.20
La	0.003	0.006	0.055	0.013	0.008	0.008	0.006
Ce	0.076	0.100	0.089	0.193	0.154	0.035	0.015
Pr	0.057	0.063	0.014	0.155	0.119	0.007	<0.005
Nd	1.14	1.84	0.089	3.1	3.5	0.033	0.053
Sm	3.59	4.38	0.052	8.9	9.1	0.021	
Eu	0.548	0.584	0.029	0.891	0.678	0.007	0.024
Gd	6.15	11.4	0.111	10.6	9.8	0.006	0.007
Tb	0.846	1.79	0.003	1.30	1.27	0.006	0.010
Dy	4.61	9.47	0.047	6.1	5.7	0.121	0.133
Ho	0.61	1.46	0.013	0.704	0.512	0.024	0.023
Er	2.02	4.73	0.036	1.88	1.57	0.092	0.066
Y	1.76	5.06	0.028	2.34	1.90	0.168	0.133
Lu	0.291	0.93	0.005	0.501	0.396	0.022	0.017

Note: * analyses for grain 1; **, analyses for grain 2; c, core; r, rim.

In sample 63, M-HREE patterns for the garnet core and rim are no different (Figure 6, sample 63). These patterns are characterized by low M-HREE contents (Gd_N 49–53, Yb_N 12–15) with a break near Ho (Ho_N/Gd_N 0.2, Yb_N/Ho_N 1.1–1.3) and a negative Eu anomaly (Eu/Eu* 0.22–0.28). The garnet is also depleted in Y (19–21 ppm) and Hf (2–3 ppm). The orthopyroxene defines steep REE patterns without the Eu anomaly. It shows overall depletion in M-HREE (Tb_N 0.17–0.30, Yb_N 0.83–1.05) and Ti (590–805 ppm). The values of D_{HREE}(Opx/Grt) are below equilibrium in the case of Tb (0.005–0.008), near equilibrium in the case of Dy (0.020–0.023), and above equilibrium in a row of Ho-Lu (0.033–0.088).

4.3. Mineral Thermobarometry

Peak mineral assemblages of the granulites studied record evidence for UHT metamorphism. The assemblage spinel + quartz with Zn-poor hercynite observed in the metapelitic rocks of the Bunger Hills [18,19] (Abdrakhmanov et al., 2021; Gulbin et al., 2022) serves as an indication of UHT [51,52] (Harley, 2008; Kelsey, 2008). Mineral indicators used to quantify UHT conditions are presented by aluminous orthopyroxene, mesoperthitic and antiperthitic feldspar, Ti-bearing quartz, and exsolutions of Fe-Ti oxides.

4.3.1. Al Solubility in Orthopyroxene

A garnet–orthopyroxene thermobarometer based on Al solubility in orthopyroxene co-existing with garnet is widely used to estimate the peak temperatures of UHT metamorphism [53–61] (Harley, 1985; McFarlane et al., 2003; Brandt et al., 2003; Tsunogae et al., 2004; Ishii et al., 2006; Tadokoro et al., 2007; Santosh et al., 2007; Bhandari et al., 2011; Sukhorukov et al., 2018). It is considered that this thermobarometer is preferred over a garnet–orthopyroxene Fe-Mg exchange thermometer due to the slower intergranular diffusivity of Al as compared with Mg and Fe [25] (Kelsey, Hand, 2015). In the case of the granulites studied, the peak temperature calculated for the garnet–orthopyroxene assemblage with the Al-in-orthopyrexene thermobarometer of Harley and Green (1982) [34] is ranged in 840–955 °C at 5–7 kbar in sample 15 (X_{Al}^{M1} 0.13–0.17 apfu), 880–930 °C at 5–6 kbar in sample 61 (X_{Al}^{M1} 0.017–0.18 apfu), 930–970 °C at 6–7 kbar in sample 63 (X_{Al}^{M1} 0.18–0.19 apfu), and

750–800 °C at 5–7 kbar in sample 116 (X_{Al}^{M1} 0.7 apfu). The Grt-Opx Fe-Mg thermometer of Lee and Ganguly (1988) [35] gives similar or smaller temperatures (Table 4).

Table 4. Representative analyses of orthopyroxene (wt%) and the results of thermobarometry calculations.

Sample	15	15	61	61	63	63	116	116
Analysis	**3-1 ***	**045 ****	**013 ****	**025 ****	**001 ****	**004 ****	**3-2 ***	**4-5 ***
SiO_2	46.46	47.36	48.90	49.29	48.50	48.01	47.79	47.49
Al_2O_3	9.03	8.72	8.24	7.98	8.88	9.22	6.07	6.05
FeO *	24.56	25.19	21.72	20.31	22.55	23.10	26.69	27.56
MnO	0.00	0.12	0.58	0.59	0.19	0.00	0.33	0.35
MgO	19.77	18.38	20.37	21.22	19.79	19.53	19.16	18.54
CaO	0.00	0.00	0.20	0.06	0.00	0.00	0.00	0.00
Total	99.82	99.77	100.01	99.45	99.91	99.86	100.04	99.99
Si	1.735	1.784	1.814	1.828	1.805	1.790	1.802	1.799
Al	0.398	0.387	0.360	0.349	0.390	0.405	0.270	0.270
Fe^{3+}	0.132	0.045	0.012	0.000	0.001	0.015	0.127	0.132
Fe^{2+}	0.635	0.748	0.662	0.630	0.701	0.705	0.715	0.741
Mn	0.000	0.004	0.018	0.019	0.000	0.000	0.011	0.011
Mg	1.100	1.032	1.126	1.173	1.098	1.085	1.076	1.047
Ca	0.000	0.000	0.008	0.002	0.000	0.000	0.000	0.000
Total	4.000	4.000	4.000	4.000	4.000	4.000	4.000	4.000
X_{En}	0.589	0.565	0.623	0.650	0.610	0.601	0.561	0.545
X_{Al}^{M1}	0.133	0.171	0.174	0.177	0.194	0.195	0.072	0.069
X_{Py}	0.397	0.350	0.401	0.401	0.382	0.382	0.333	0.333
X_{Grs}	0.010	0.011	0.029	0.029	0.018	0.018	0.034	0.034
X_{Sps}	0.014	0.011	0.047	0.047	0.011	0.011	0.027	0.027
K_{D1}	0.118	0.147	0.157	0.159	0.165	0.166	0.074	0.071
K_{D2}	2.094	2.329	2.178	2.426	2.408	2.318	2.326	2.180
P_{ref}, kbar	5.0–7.1	5.0–7.0	5.1–7.0	5.0–7.0	6.1–7.0	6.0–7.0	5.1–7.1	5.0–7.1
T_{GH82}, °C	840–900	895–955	885–945	875–935	935–965	935–970	750–800	750–800
T_{LG88}, °C	945–960	870–880	960–970	890–900	860–870	885–890	905–915	950–960

Note: * analyses obtained using JEOL JSM-7001F SEM at SPMU, ** using JEOL JSM-6510LA SEM at IPGG RAS. Back-scattered electron (BSE) images showing crystals of orthopyroxene with points of microprobe analyses are provided in Figure S5. For each sample, analyses with the highest Al_2O_3 contents are given. Structural formulae normalized to 4 cations and 12 charges. Mole fractions for orthopyroxene are as follows: $X_{En} = Mg/(Mg + Fe)$; $X_{Al}^{M1} = Si - (2 - Al)$ [62] (Pattison et al., 2003). Mole fractions for garnet are as follows: $X_{Py} = Mg/(Mg + Fe + Mn + Ca)$; $X_{Grs} = Ca/(Mg + Fe + Mn + Ca)$; $X_{Sps} = Mn/(Mg + Fe + Mn + Ca)$. Garnet analyses with the highest pyrope content were used for the calculations. $K_{D1} = [X_{Al}^{M1}(1 - X_{Al}^{M1})/(1 - X_{Grs})]^3$; $K_{D2} = (Fe/Mg)^{Grt} \times (Mg/Fe)^{Opx}$. T_{GH82}, temperature estimated with Harley and Green (1982) thermobarometer [34]; T_{LG88}, with Lee and Ganguly (1988) thermobarometer [35]; P_{ref}, the reference pressure.

In addition to the Al_2O_3 content in orthopyroxene, one more indicator of P-T conditions is the temperature- and pressure-dependent relationship between X_{Al}^{M1} and X_{En}. The P-T grid with X_{Al}^{M1} and X_{En} isopleths was calculated by Hensen and Harley (1990) [63] for the FMAS (Grt-Opx-Cord-Qz) assemblage using experimental data and assuming the isobaric orientation of X_{Mg} isopleths in garnet in the P-T space. This grid was transformed into the X_{Al}^{M1} vs. X_{En} plot by Tateish et al. (2004) [64], who applied it for thermobarometry. Figure 7 shows such a plot for the rocks studied. Based on plotted isotherms and isobars, one can conclude that the orthopyroxene with the highest aluminum content having X_{En} values of 0.58–0.65 is equilibrated in a P-T range of >900 °C and 6–8 kbar. At these conditions, orthopyroxene is in equilibrium with garnet containing a 0.44–0.48 mole fraction of pyrope. That is more than observed (≤0.40), which is due partly to the presence of minor Ca and Mn in the garnet and to the partial loss of Mg occurring when cooling.

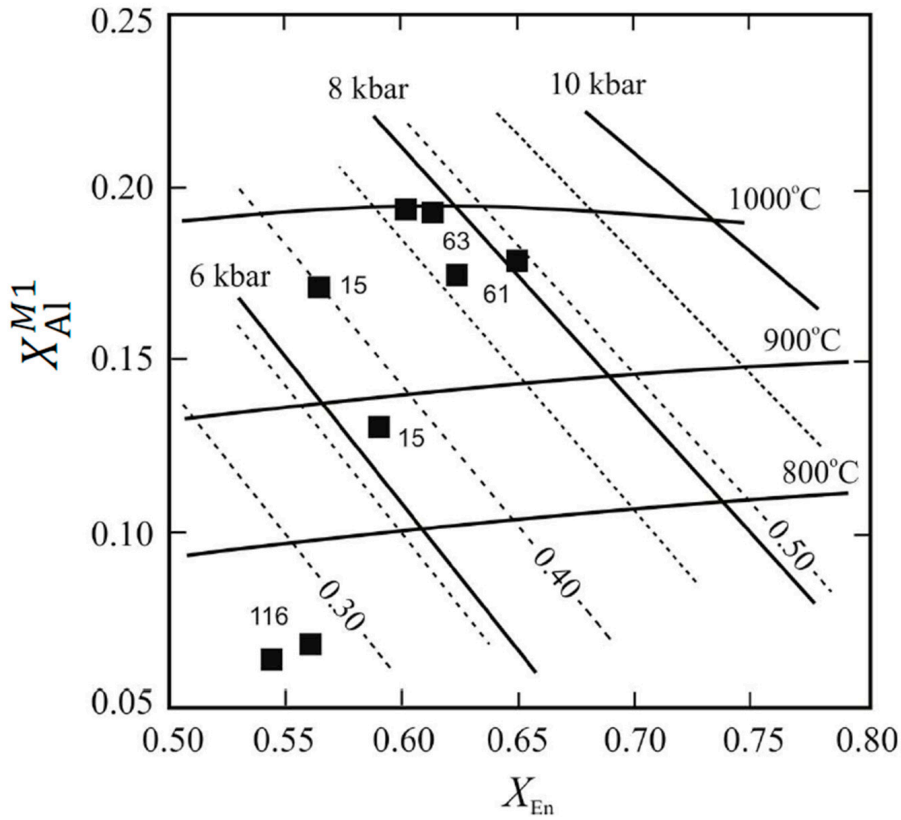

Figure 7. X_{Al}^{M1} vs. X_{En} plot with isotherms and isobars from [63] Hensen and Harley (1990). Modified after [64] Tateishi et al. (2004). Dashed lines indicate X_{Mg} isopleths in garnet. Numbers near composition points correspond to the numbers of the samples in Table 4.

4.3.2. Ternary Feldspar Geothermometry

Ternary feldspar geothermometry is based on the determination of the pre-exsolution feldspar composition by the Hokada (2001) method [39] followed by its plotting on the An-Ab-Or ternary plot with sulvus isotherms. Despite the problematic nature of this approach [51] (Harley 2008), it has been applied to support UHT evidence for many granulite terranes [56,57,61,65–68] (Tsunogae et al., 2004; Ishii et al., 2006; Pilugin et al., 2009; Martignole, Wang, 2010; Jiao, Guo, 2011; Sukhorukov et al., 2018; Nanne et al., 2020). Table 5 displays the results of the calculations of one-phase feldspar compositions performed using this technique for the mesoperthic (host/lamellae = 74/26 vol.%) and antiperthitic (host/lamellae = 77/23 vol.%) grains in sample 63. Their re-integrated compositions are $Ort_{0.62}Ab_{0.32}An_{0.06}$ and $Ab_{0.64}An_{0.17}Ort_{0.19}$, respectively. On the ternary plot with sulvus curves from [40] Fuhrman and Lindsey (1988) and [69] Elkins and Grove (1990) (Figure 8), these compositions give similar temperatures exceeding 900 °C (ranging from 900 to approximately 930 °C). Obviously, mesoperthitic and antiperthitic feldspar are equilibrated at these conditions. Note, additionally, that two compositions measured by area scan SEM analysis show different temperatures (>900 and ~800 °C). Such a difference may be related to the systematic matrix-effects error of the area scan microprobe analysis as previously noted by Hokada (2001) [39] and confirms the merits of his method.

Table 5. Representative analyses of feldspar (wt%) and re-integrated feldspar compositions.

Sample				**63**				
Feldspar		**Mesoperthitic**				**Antiperthitic**		
Domain	**re-int (scan)**	**host**	**lamellae**	**re-int (calc)**	**re-int (scan)**	**host**	**lamellae**	**re-int (calc)**
Analysis	**054**	**051**	**050**		**055**	**059**	**056**	
SiO_2	65.30	64.88	62.72	64.29	64.73	64.36	64.87	64.48
Al_2O_3	19.26	18.82	23.48	20.09	22.13	23.06	18.76	22.06
CaO	0.48	0.00	4.53	1.23	2.98	4.72	0.00	3.62
Na_2O	3.18	1.61	8.78	3.56	7.12	9.38	1.67	7.58
K_2O	12.25	14.49	12.25	10.62	3.77	0.07	14.31	3.39
BaO	0.00	0.20	0.00	0.15	0.00	0.00	0.00	0.00
Total	100.47	100.00	99.75	99.93	100.73	101.59	99.61	101.13
Si	2.967	2.984	2.780	2.927	2.860	2.803	2.988	2.844
Al	1.032	1.020	1.227	1.078	1.152	1.184	1.019	1.147
Ca	0.023	0.000	0.215	0.060	0.141	0.220	0.000	0.171
Na	0.280	0.144	0.755	0.314	0.610	0.792	0.149	0.648
K	0.710	0.850	0.014	0.617	0.212	0.004	0.841	0.191
Ba	0.000	0.004	0.000	0.003	0.212	0.000	0.000	0.000
Total	5.012	5.002	4.990	4.999	4.975	5.003	4.997	5.002
An	0.023	0.000	0.219	0.061	0.146	0.217	0.000	0.169
Ab	0.276	0.144	0.767	0.317	0.633	0.779	0.151	0.642
Ort	0.701	0.856	0.014	0.622	0.221	0.004	0.849	0.189
Vol,%		73.6	26.4			77.3	22.7	
Wt,%		72.8	27.2			76.65	23.35	

Note: analyses obtained using JEOL JSM-6510LA SEM at IPGG RAS; re-int (scan), re-integrated feldspar compositions measured by area scan SEM analysis; re-int (calc), re-integrated feldspar compositions determined by Hokada (2001) method [39]. Vol,%, volume proportions of lamellae and host domains; Wt,%, weight percentages converting from volume proportions using densities of alkali feldspar (2.57 g/cm^3) and plagioclase (2.67 g/cm^3).

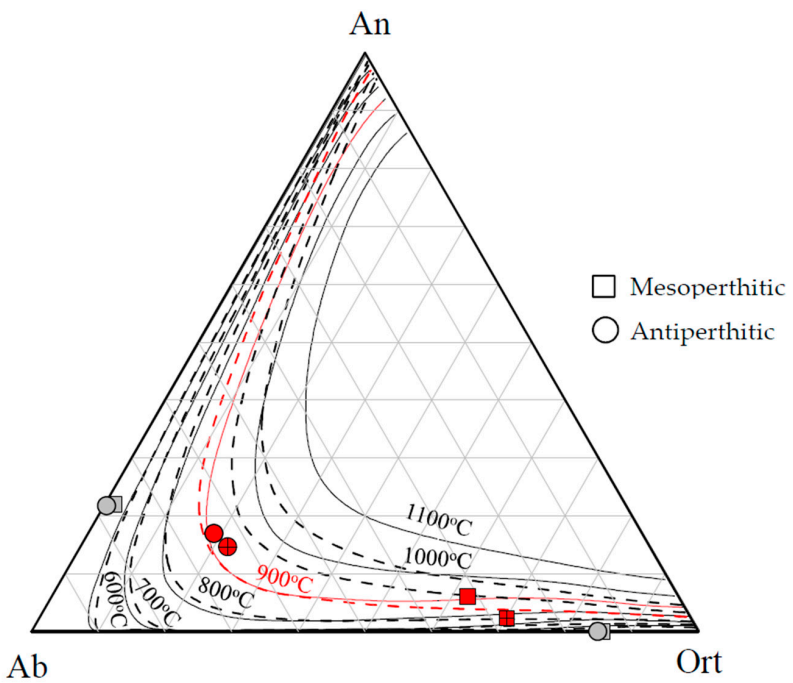

Figure 8. Ternary plots of the exsolved (gray) and re-integrated (red, determined by Hokada (2001) method [39]; red, crossed, measured by area scan SEM analysis) feldspar compositions for sample 63 along with the solvus curves calculated for 600–1100 °C at 6 kbar with the WinFeldth software [70] (Yavuz, Yavuz, 2022) using the models of Fuhrman and Lindsey (1988) [40] (solid lines) and Elkins and Grove (1990) [69] (dashed lines).

4.3.3. Ti-in-Quartz Geothermometry

Unlike the above methods, Ti-in-quartz geothermometry has not yet found widespread use to study granulite facies rocks [25] (Kelsey, Hand, 2015). This is partly due to the fact that the calibrations of the Ti-in-quartz geothermometer taking into account the pressure appeared relatively recently [36,37] (Thomas et al., 2010; Huang, Audétat, 2012). The robustness of this geothermometer against the loss of Ti during cooling is also a subject of discussion [25] (Kelsey, Hand, 2015). It should be noted in this regard that the high diffusivities of Ti in quartz at temperatures over 900 °C [71] (Cherniak et al., 2007) are compensated by the rutile exsolution which is often observed in quartz from granulites and prevents the diffusive loss of Ti. For this reason, several authors consider Ti-in-quartz geothermometry as a promising tool to identify peak temperature at UHT conditions [72–74] (Sato, Santosh, 2007; Adachi et al., 2010; Ewing et al., 2013).

As shown in Table 2, the Ti-in-quartz peak temperature for the studied granulites varies in the range of 760–810 °C being calculated with the Thomas et al. (2010) calibration [36] and in the range of 950–1010 °C being calculated using the Huang and Audétat (2012) calibration [37]. The high variability of the obtained estimates relates to the different solubility of Ti in quartz according to experiments performed by various researchers. It was previously shown that the Huang and Audétat (2012) calibration [37] overestimates temperature [74] (Ewing et al., 2013). Nevertheless, in this work, we give preference to the Huang and Audétat (2012) temperatures for two reasons: (1) they agree better with those obtained by other mineral geothermobarometers, and (2) they match well with the results of phase equilibrium modeling (see the next section). Remembering that the studied quartz contains the preferable oriented exsolved needles of rutile and spinel [19] (Gulbin et al., 2022), and assuming that the analytical spot used for the analyses has re-integrated the composition of pre-exsolved quartz, these temperatures can be considered as the peak ones provided that all available Ti enters into the structure of quartz at high temperature and that it is exsolved into oxide phases when the temperature decreases, which limits the diffusion and partitioning of Ti between quartz and co-existing minerals.

4.3.4. Fe-Ti Oxide Solvus Geothermometry

Titaniferous magnetite–ilmenite intergrowths are common in metapelitic granulite and are interpreted as a product of the oxidation of high temperature magnetite–ulvöspinel solid solutions [75] (Buddington, Lindsley, 1964). Fe-Ti oxide geothermometry/oxygen fugacity barometry, based on this exsolution phenomenon, is an important tool for determining the conditions of metamorphism. Peak temperatures obtained using this geothermometry for granulite facies rocks do not exceed 900 °C as a rule [76–78] (Bohlen, Essene, 1977; Rollinson, 1980; Harlov, 2000) and often decrease to 600–800 °C because of the re-equilibration of minerals during cooling [75] (Buddington, Lindsley, 1964). The ulvöspinel content of magnetite does not rise higher than 47 mol.% at these conditions. The exception is the granulite gneisses from Doubtful Sound, New Zealand, composed of lamellae of magnetite with up to 53 mol.% of ulvöspinel and formed at a temperature >1000 °C [79] (Oliver, 1978). Against this background, the metapelitic granulites of the Bunger Hills are of great interest as they contain flame-like exsolutions of titaniferous magnetite (X_{Usp} 0.38–0.46) and ulvöspinel (X_{Usp} 0.55–0.78) occurring in intergrowths with ilmenite, corundum, and needle-like rutile (Table S6). The peak Fe-Ti oxide temperature obtained for sample 63 in which such exsolutions were found, with the FeTi-oxide geothermometer/oxygen barometer following Andersen and Lindsley (1985) and Sauerzapf et al. (2008), exceeded 900 °C (Table S6) [80,81]. Furthermore, oxygen fugacity was buffered under redox conditions corresponding to the Ni-NiO equilibrium [18] (Abdrakhmanov et al., 2021).

4.4. Phase Equilibrium Modeling

Isochemical Diagrams

The bulk rock compositions (Table 1) were used to construct P-T isochemical phase diagrams. Further, they are considered for selected groups of granulites.

Sample 2a serves as an example of garnet–sillimanite–cordierite gneiss. It contains spinel, rutile, and biotite which occur in the matrix and as euhedral inclusions in the garnet. Sillimanite is represented by the second and third generations. There is no plagioclase in the rock because of the low content of CaO (0.30 wt%). The isochemical phase diagram for this sample is presented in Figure 9a. The plot is calculated for the system MnNCKFMASHT (MnO-Na_2O-CaO-K_2O-FeO-MgO-SiO_2-H_2O-TiO_2) due to the absence of magnetite in the rock. The interpreted peak mineral assemblage here is garnet–cordierite–spinel–K-feldspar–ilmenite–quartz. It is calculated to be stable at 5.6–6.6 kbar and >940 °C provided there is very low water activity. The predicted mineral assemblage field overlaps with an area where Mg-in-garnet isopleths corresponding to the observed X_{Mg}^{Grt} values (0.29–0.31) are located. This result is applicable for the assemblage including varieties of the hercynite–spinel series. However, because the observed spinel contains minor Zn and Cr, the stability of the spinel–quartz–cordierite–garnet equilibrium may expand toward lower temperatures [82] (Nichols et al., 1992). The garnet started to crystallize at ~730 °C and ~7 kbar in the field of the rutile- and biotite-bearing assemblage provided there was relatively high water activity. This is evidenced by the presence of rutile and biotite inclusions in the garnet. Their crystallization temperature was determined with the Henry et al. (2005) Ti-in-biotite geothermometer [38] (details see in Table S3). The early prograde evolution comprised isobaric heating in the field of sillimanite and cordierite stability. The temperature increase resulted in the partial melting of the rock accompanied with a loss of water dissolving in the melt. Peak temperature was followed by isobaric cooling in the field of cordierite. The appearance of late-stage sillimanite and biotite replacing cordierite coupled with Ti-in-biotite geothermometry suggests that, at some point, the pressure increased slightly during the retrograde history.

Samples 75 and 78 provide examples of garnet–cordierite gneiss. Because these rocks contain magnetite as a minor phase, the system MnNCKFMASHTO (MnO-Na_2O-CaO-K_2O-FeO-MgO-SiO_2-H_2O-TiO_2-O_2) was used for thermodynamic modeling. As Figure 9c,e show, the peak assemblage garnet–cordierite–spinel–K-feldspar–plagioclase–ilmenite–quartz is constrained to approximately 6–7 kbar and >950 °C under low water activity. This temperature estimate is confirmed by data of the Huang and Audétat (2012) Ti-in-quartz thermobarometer [37]. In sample 75, the presence of sillimanite and biotite inclusions in the garnet indicates the early stage of metamorphic crystallization in the field of the garnet–sillimanite–biotite–plagioclase–ilmenite assemblage (Figure 9b). In sample 78, this stage is also expected (Figure 9d). The geothermometry of the biotite inclusions gives a temperature of ~760 °C for this point on the prograde P-T path. Under relatively high water activities, it suggests isobaric heating in the field of cordierite at 6–6.5 kbar up to partial melting conditions. After peak temperature metamorphism, isobaric cooling at 5–5.5 kbar can be expected in both samples. This cooling presumably resulted in a decrease in the Mg content in the garnet, which caused the measured X_{Mg}^{Grt} values (0.30–0.34) to be lower than those calculated for the peak assemblage (0.34–0.36). The final phase of the retrograde P-T path is recorded by the appearance of late-stage sillimanite which serves as an indicator of increasing pressure (Figure 4g,h).

Samples 15 and 63 are examples of garnet–cordierite–orthopyroxene gneiss. In both samples, isochemical phase diagrams in the system MnNCKFMASHTO, contoured for X_{Mg} in garnet (0.36–0.40) and X_{Al}^{M1} in orthopyroxene (0.18–0.20) and combined with mineral thermobarometry, were used to constrain the peak metamorphic conditions. As seen from Figure 10, mineral compositional isopleths corresponding to the measured composition of garnet and orthopyroxene overlap within the Grt-Crd-Opx-Pl-Kfs-Ilm assemblage field at 5–6 kbar and 920–970 °C. These pressures and temperatures agree well with data of the Harley and Green (1982) Al-in-orthopyroxene (5–6.5 kbar, 910–950 °C) and Huang and Audétat (2012) Ti-in-quartz (5–6.5 kbar, 880–920 °C) thermobarometers [34,37]. The prograde P-T path started in the sillimanite or sillimanite–biotite stability field at 6–6.5 kbar and ~800 °C, which is indicated by the sillimanite and biotite inclusions in the garnet. Further, isobaric heating took place in the fields of the Grt-Sil-Opx-Pl-Kfs-Ilm and Grt-Crd-

Opx-Pl-Kfs-Ilm assemblages until the rocks had experienced partial melting which was favored by the relatively high water activity. The retrograde P-T path contained nearly isobaric cooling at 5–5.5 kbar followed by a slight increase in pressure (up to 6 kbar). As a result, late-stage sillimanite and quartz–biotite symplectite were formed, which replaced the minerals of the peak assemblage.

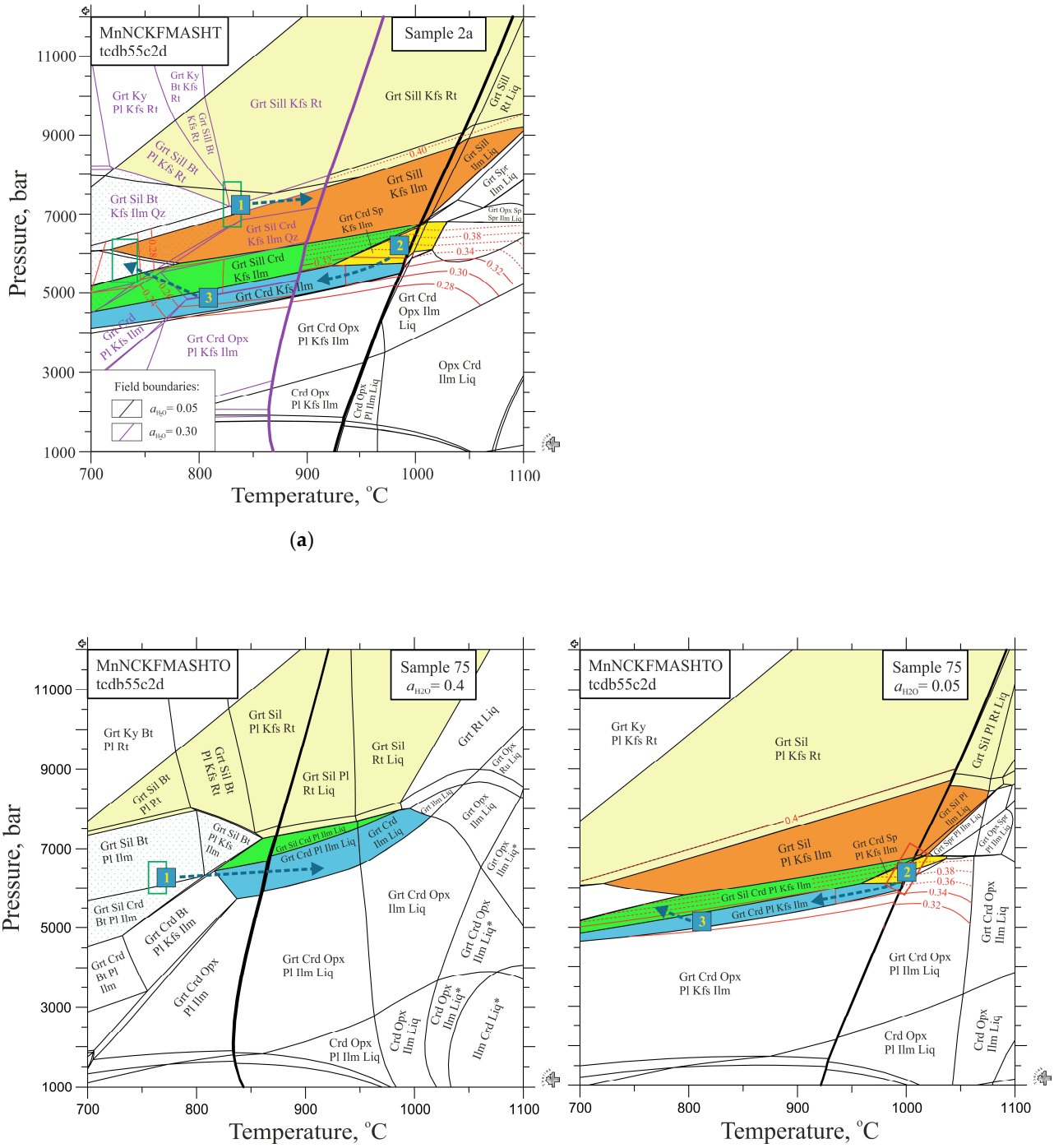

Figure 9. *Cont.*

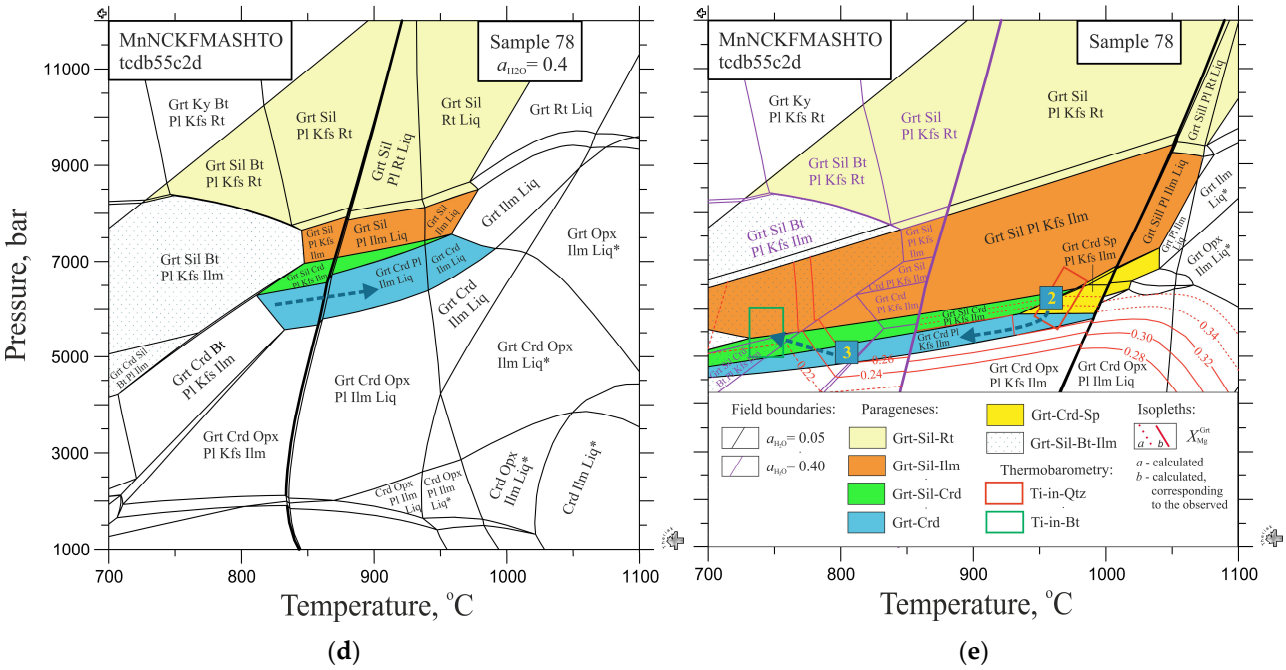

(**d**) (**e**)

Figure 9. Isochemical P-T phase diagram calculated for garnet–sillimanite–cordierite and garnet–cordierite gneiss. (**a**) Sample 2a; (**b**,**c**) sample 75; (**d**,**e**) sample 78. The bulk compositions used for calculations are given in Table 1. Thin black and purple lines delimit mineral assemblage fields for different water activities. Solid bold lines correspond to the solidus. Solid and dashed red lines with numbers indicate X_{Mg} isopleths in garnet. All mineral assemblages contain quartz (sample 2a), or quartz and magnetite (samples 75, 78), except those marked by a star which are quartz-free. Liq, melt. The colored rectangle outlines of the P-T conditions are derived from mineral thermobarometry. Blue and brown arrows represent the inferred P-T path sections for the prograde (1) and retrograde (2, early; 3, late) phases of metamorphism.

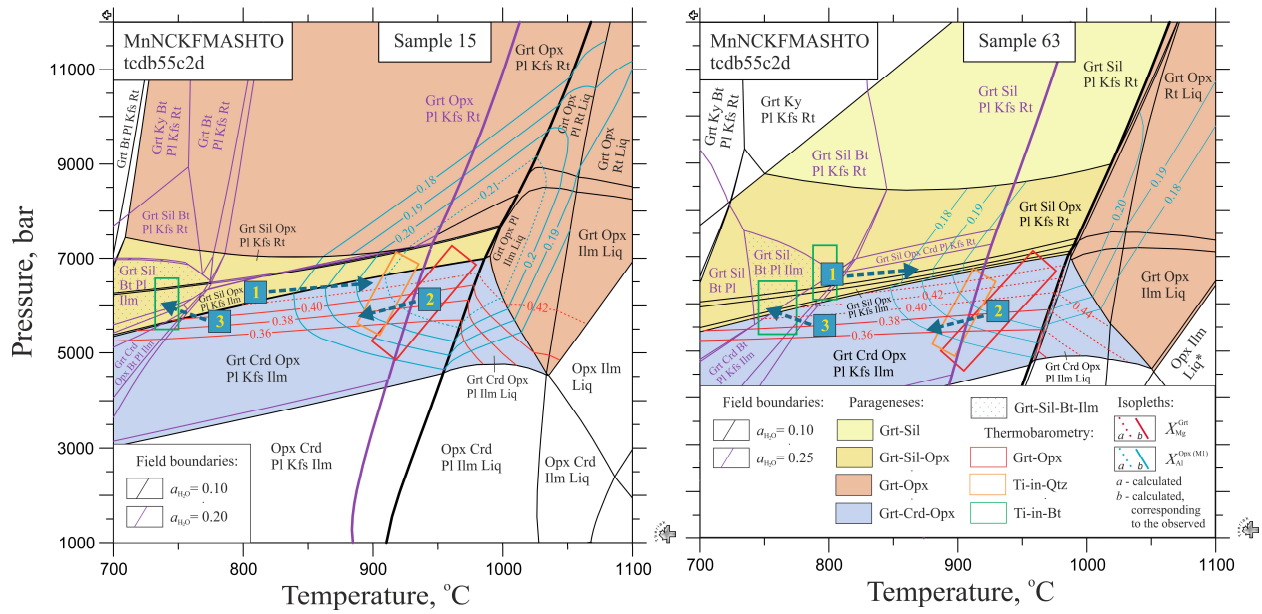

Figure 10. Isochemical P-T phase diagram (pseudosection) calculated for garnet–orthopyroxene–cordierite gneiss. The bulk compositions used for calculations are given in Table 1. All mineral assemblages contain quartz and magnetite except those marked by a star which are quartz-free. See legend to Figure 9 for details.

5. Discussion

5.1. Mineral Evidence for a Two-Phase Metamorphic History

Mineral thermobarometry and isochemical phase diagram modeling support the idea that the granulites in the Bunger Hills experienced intermediate pressure (6–7 kbar) UHT metamorphism. The highest temperatures for these rocks are recorded by orthopyroxene associated with garnet (930–970 °C), quartz (940–980 °C), feldspar (900–930 °C), and Fe-Ti oxides (>900 °C), which confirm that the assemblage Zn-poor spinel + quartz occurring in the granulites is indicative of extreme thermal conditions. This inferred peak assemblage, including additionally garnet, cordierite, K-feldspar, and ilmenite (±magnetite), is modeled to be stable at 6–7 kbar and 940–1030 °C if the water activity is low and spinel is an intermediate variety of the hercynite–spinel series (Figure 9). The measured composition of garnet associated with spinel in the granulites may correspond to the calculated X_{Mg}^{Grt} values (0.32 in sample 2a) for the peak assemblage or may be different as a result of the Mg-Fe diffusion during cooling, which promotes decreasing X_{Mg}^{Grt} values (from 0.34–0.36 to 0.32–0.34 in samples 75 and 78). The modeling predicts that all listed minerals (except spinel) and also sillimanite are included in the pre-peak assemblage, an example of which is sample 2a. Here, it is noteworthy to repeat that, unlike the hercynitic spinel considered in the model, the spinel in the studied rocks contains minor Zn and Cr, which expands the field of its stability towards lower temperatures [82] (Nichols et al., 1992). Therefore, we assume that spinel was a part of the pre-peak assemblage too. In other words, first-generation spinel (Mg-poor and Zn-poor) could appear during prograde metamorphism, and namely this spinel forms inclusions in garnet, sillimanite, and cordierite. For garnet–sillimanite–cordierite gneiss, the prograde P-T path entirely passed through the field of the assemblage Grt-Sil-Crd-Kfs-Qz-Sp(I)-Ilm (±Mag), which is limited towards higher pressures by the rutile-in boundary (Figure 9a). The presence of ilmenite, rutile, and biotite inclusions in the garnet allows us to conclude that the P-T path started at ~7 kbar and 800–850 °C or lower temperatures under the relatively high water activity in the field of ilmenite or rutile stability. Subsequent heating occurred at a near-isobaric regime, causing the P-T path to cross the solidus, after which partial melting started. As a result, the water activity decreased greatly, and conditions for the second-generation spinel growth were created. It crystallized following the prograde reaction as follows:

$$\text{Grt} + 2\text{Sil} = \text{Sp} + \text{Crd},$$

during which garnet and sillimanite were consumed partly owing to the growth of newly formed cordierite and spinel. The reaction did not complete due to which the sillimanite was preserved. In the case of garnet–cordierite gneiss, the above scenario took place except that heating occurred in the field of the Grt-Crd-Pl-Qz-Ilm-Mag assemblage which, again, was facilitated by the increased water activity. In the case of garnet–cordierite–orthopyroxene gneiss, the prograde P-T path is inferred to begin in the field of sillimanite + biotite stability and records isobaric heating along the field of the Grt-Crd-Opx-Pl-Kfs-Qz-Ilm-Mag assemblage until peak temperature is reached (Figure 10).

The modeled retrograde P-T path implies a two-phase history: (1) initial isobaric (5–6 kbar) cooling along the field of the cordierite stability, followed by (2) cooling with compression (by ~0.5 kbar) which resulted in the pressure and temperature trajectory ending in the field of the sillimanite stability. The last segment of the P-T path (Figure 9a,c,e and Figure 10) is supported by the presence of late acicular sillimanite generation, together with biotite, replacing cordierite along grain boundaries via the reaction as follows:

$$3\text{Crd} + 2\text{Kfs} + 2\text{H}_2\text{O} = 6\text{Sil} + 2\text{Bt} + 9\text{Qz}.$$

The replacement of cordierite by late-stage sillimanite and biotite is well known (e.g., [83–85] Clarke et al., 1989; Booger, White, 2003; Halpin et al., 2007). Vernon (1979) [86] describes late fibrolitic sillimanite replacing cordierite, K-feldspar, andalusite, biotite, etc., in high-grade migmatitic gneisses, and summarizes hypotheses for the origin of such

sillimanite in metamorphic rocks proposed by different researchers [87] Vernon, 1979, and reference therein. He argues in favor of the view that the formation of late sillimanite was controlled by local metasomatic processes (the action of acidic aqueous solutions containing the Al_2SiO_5 component on rock-forming minerals). In contrast, we focus attention on phase reactions occurring in isochemical systems, and interpret the breakdown of cordierite to sillimanite to reflect changes in P-T conditions. Arguments for this mechanism are that (1) late sillimanite replaces only cordierite and no other minerals, and (2) in the constructed phase diagram, the sillimanite stability field is located above the cordierite stability field. Moreover, late sillimanite is associated with biotite which replaces all pre-existing minerals. Therefore, as the modeling and Ti-in-biotite geothermometry predict, the appearance of late sillimanite and biotite can be accounted for by an increase in pressure and water activity during the final stage of retrograde cooling.

REE distributions between garnet and orthopyroxene provide additional evidence of the behavior of minerals at the prograde and retrograde stages. According to trace element data, two types of garnet are identified. Type-1 garnet from sample 15 is unzoned from core to rim and displays strong enrichment in Y, M-HREE, and Hf (Table 3, Figure 6, sample 15). Type-1 garnet coexists with orthopyroxene also enriched in M-HREE. The values of the orthopyroxene/garnet M-HREE distribution coefficients are close to equilibrium values 0.01–0.03 [50] (Harley, Kelly, 2007), which indicates orthopyroxene–garnet partitioning. Type-2 garnet from sample 63 is also unzoned, but exhibits strong depletion in Y, M-HREE, and Hf (Table 3, Figure 6, sample 63). Type-2 garnet coexists with orthopyroxene depleted in M-HREE. The D_{HREE}(Opx/Grt) values are noticeably higher in comparison with those expected for equilibrium. Intermediate-type garnet from sample 61 shows moderate depletion in M-HREE in the case of the unzoned grain (Figure 6, sample 63, grain 1) and stronger depletion in M-HREE within the rim relative to the core in the case of grains with zoning (Figure 6, sample 63, grain 2). This type of garnet coexists with orthopyroxene depleted in M-HREE. The D_{HREE}(Opx/Grt) values here are below equilibrium. Both types of garnet are somewhat similar to those determined in the granulite of the Bunger Hills by Tucker et al. (2018) [17]. The authors suggested that the difference between HREE-enriched garnet and HREE-depleted garnet is due to the former having grown prior to zircon crystallization, whereas the latter grew after zircon crystallization ceased in the HREE-depleted environment. Following this assumption, we believe that the garnet and orthopyroxene in sample 15 are earlier and could have grown at the prograde stage, before reaching peak conditions, which caused the low X_{Al}^{M1} values (0.8–0.11, Figure S6). Their crystallization took place in the M-HREE- and Hf-saturated medium, which contributed to the partitioning between the coexisting minerals. Furthermore, the garnet and orthopyroxene in samples 61 and 63 are later and could have grown at the peak stage, which caused the high X_{Al}^{M1} values (0.11–0.18, Figure S6). Their crystallization happened in the medium undersaturated in M-HREE and Hf, which was incorporated in the zircon, due to which the garnet and orthopyroxene were not equilibrated.

5.2. P-T Evolution and Tectonic Setting

The main conclusion of the previous section is that the P-T path for the Bunger Hills granulites corresponds to a tight clockwise trajectory that reflects a two-phase history: (1) near-isobaric heating followed (2) first by near-isobaric and then slightly up-pressure cooling. On the basis of currently available zircon and monazite U–Pb geochronology, these two episodes can be related to two late Mesoproterozoic tectono-thermal events, one at ca. 1220–1180 Ma when UHT metamorphism occurred [17] (Tucker et al., 2018) and the other at ca. 1200–1150 Ma when gabbroic and charnockitic plutons were emplaced [16,17] (Sheraton et al., 1992; Tucker et al., 2017). Both ages correlate with Stage-2 of the evolution of the Albany–Fraser Orogen, the westernmost part of which the Bunger Hills are believed to be [10–12] (Sheraton et al., 1993; Clark et al., 2000; Morrissey et al., 2017).

Tectonic settings responsible for the granulite facies metamorphism are subdivided into two principal types: collisional and subduction-accretionary [21–25,87] (Bohlen, 1987; Harley, 1989; Collins, 2002a, 2002b; Brown, 2007; Kelsey, Hand, 2015). Granulites formed in collisional orogens are characterized by "near-isothermal decompression" clockwise P-T paths, indicating post-collisional thinning of the overthickened continental crust. In this environment, a heat source for metamorphism may be radiogenic crustal heat production [88] (England, Thompson, 1984). Granulites formed in accretionary orogens and associated with subduction in continental arcs and back-arc systems show "near-isobaric cooling" clockwise or anticlockwise P-T paths, reflecting a dominantly extensional regime involved in crustal thinning. In this environment, the main heat source is the mantle-induced magmatic accretion at the lowermost crust [89,90] (Wells, 1980; Sadinford, Powel, 1986). There are two types of accretionary settings: terrain accretionary and extensional accretionary [22–24] (Collins, 2002a, 2002b; Brown, 2007). The latter is especially favorable for low-pressure granulite facies metamorphism and associated with mafic to felsic magmatism. Although there was a prolonged lithospheric extension during the accretionary orogenic history, short contractional episodes sporadically interrupted the extension leading to crustal thickening [22,23] (Collins, 2002a, 2002b).

The P-T path inferred for the Bunger Hills granulites is not compatible with collisional tectonics, but is similar to the pressure and temperature trajectories suggested for the extensional accretionary setting [21] (Harley, 1989). It may be of interest to discuss this conclusion in a regional context. The Albany–Fraser Orogen, which includes the Bunger Hills region as its westernmost continuation (Figure 1), is regarded as a response to the Late Mesoproterozoic Rodinia assembly (e.g., [13] Smits et al., 2014). Early studies linked its tectonic history with continental collision occurring between 1300 and 1100 Ma [91] (Myers, 1990). Later, Albany–Fraser Orogeny was divided into two stages corresponding to two major compressional events: (1) collision at ca. 1345–1260 Ma followed by (2) intracratonic reactivation at ca. 1215–1140 Ma [11] (Clark et al., 2000). Recently, the emphasis in the interpretation of the tectonic evolution of the Albany–Fraser Orogen has shifted from the compressional to the extensional regime, which may explain the tectonic processes that developed in the southeastern margin of the West Australian Yilgarn Craton [12, 92,93] (Clark et al., 2014; Spaggiari et al., 2015; Morrissey et al., 2017). In the proposed scenario, Stage-1 metamorphism and magmatism at ca. 1330–1280 Ma took place in the back-arc system involved after the lateral accretion of an oceanic arc to the craton edge. This event is recorded mainly along the eastern margin of the Albany–Fraser Orogen, an example of which is the Windmill Islands region in the Antarctic segment of the belt [12] (Morrissey et al., 2017). Following Stage-1, a period of tectonic compression occurred at ca. 1250–1210 Ma, which gave way to the Stage-2 orogenic activity that happened throughout the Albany–Fraser Orogen as well as in the adjacent Musgrave Province. The last event occurred at ca. 1225–1140 Ma and is marked by high-grade metamorphism and voluminous charnockite magmatism which are interpreted to indicate high heat flow and partial melting of the thinned crust related to the extensional setting [12,94] (Smithies et al., 2011; Morrissey et al., 2017). This tectono-thermal environment is very likely characteristic of the Bunger Hills where granulite facies metamorphism occurred at 1220–1180 Ma [17] (Tucker et al., 2018) and mafic to felsic plutons (including charnockite intrusions) were emplaced at 1200–1150 Ma [15,16] (Sheraton et al., 1992; Tucker et al., 2017). Another piece of evidence of the crustal extension in the area is a ductile deformation (D_1) synchronous with peak metamorphism, which produced the dominant foliation and boudinage of mafic layers in the granulite sequence, and is attributed to extensional tectonics [20,30] (Stüwe, Powel, 1989; Sheraton et al., 1995). It can be assumed that the near-isobaric heating prograde P-T trajectory at mid-crustal levels predicted for the Bunger Hills is associated with this tectonic phase of the orogenic history. The extensional deformation (D_1) was followed by the major compressional deformation (D_2 after [20] Stüwe, Powel, 1989; D_2–D_3 after [30] Sheraton et al., 1995), which caused the folding of the sequence. The researchers linked this compressional deformation with the post-peak metamorphic evolution [20] (Stüwe,

Powel, 1989). It is quite possible, therefore, that the near-isobaric to slightly up-pressure cooling retrograde P-T path obtained in this study reflects the late-orogenic contractional event responsible for crustal thickening. This agrees well with the tectonic model of [22,23] Collins (2002a, 2002b), which states that once the thinned crust in the accretionary orogen thickens during the short-lived contractional phases of orogeny, it immediately cools.

6. Conclusions

Petrographic observations and mineral thermobarometry show that granulites of the Bunger Hills experienced UHT metamorphism at mid-crustal levels (ca. 20–23 km). The tight clockwise P-T path constructed from the isochemical phase diagram modeling is characterized by near-isobaric heating at 6–7 kbar to ~940–1030 °C followed by near-isobaric to slightly up-pressure cooling at 5–6 kbar to ~750 °C. The prograde P-T trajectory passed through the stability fields for the assemblages Grt ± Sil-Crd-Ilm and Grt-Crd-Opx-Ilm, usually without crossing phase boundaries between ilmenite and rutile, which constrained the peak pressure conditions. The retrograde section of the P-T path occurred in the field of the cordierite stability, wherein cordierite was partly replaced by late sillimanite towards the end of the cooling phase, indicating increased pressure. This metamorphic history contrasts with the down-pressure P-T path reported for the Bunger Hills earlier, and is almost identical to the tectono-thermal evolution in the extensional setting proposed for Stage-2 of the Mesoproterozoic Albany–Fraser Orogeny. To be more specific, the peak assemblages of the studied granulites are assumed to be associated with the main extensional phase of orogeny, whereas the post-peak assemblages may be related to the late-orogenic contractional event responsible for crustal thickening.

Supplementary Materials: The following supporting information can be downloaded at: https://www.mdpi.com/article/10.3390/min14050488/s1, Table S1: Representative analyses of core and rim of garnet and orthopyroxene (wt%) in metapelitic granulite of the Bunger Hills; Table S2: Representative analyses of cordierite (wt%) in metapelitic granulite of the Bunger Hills; Table S3: Representative analyses of biotite (wt%) in metapelitic granulite of the Bunger Hills and the results of thermobarometry calculations; Table S4: Representative analyses of K-feldspar and plagioclase (wt%) in metapelitic granulite of the Bunger Hills; Table S5: Representative analyses of spinel (wt%) in metapelitic granulite of the Bunger Hills; Table S6: Representative analyses of titaniferous magnetite and ilmenite (wt%) in sample 63 and the results of thermobarometry calculations; Figure S1: Back-scattered electron (BSE) images of garnet and orthopyroxene and rim–core–rim zoning profiles; Figure S2: Back-scattered electron (BSE) images showing occurrences of analyzed biotite in granulite; Figure S3: Back-scattered electron (BSE) images showing occurrences of analyzed feldspars in granulite; Figure S4: Back-scattered electron (BSE) images showing occurrences of analyzed spinel in granulite; Figure S5: Back-scattered electron (BSE) images showing crystals of orthopyroxene with points of microprobe analyses used for thermobarometry; Figure S6: Back-scattered electron (BSE) images showing crystals of garnet and orthopyroxene in which major and trace element compositions were measured.

Author Contributions: Conceptualization, I.A.A. and Y.L.G.; methodology, all authors; field works, I.A.A.; software, all authors; validation, Y.L.G. and S.G.S.; formal analysis, Y.L.G.; investigation, I.A.A. and Y.L.G.; resources, S.G.S. and O.L.G.; data curation, Y.L.G.; writing—original draft preparation, I.A.A. and Y.L.G.; writing—review and editing, S.G.S.; visualization, I.A.A. and Y.L.G.; supervision, Y.L.G.; project administration, Y.L.G. All authors have read and agreed to the published version of the manuscript.

Funding: This research received no external funding.

Data Availability Statement: Data available within the article.

Acknowledgments: The authors thank Irina Gembitskaya, Evgeny Potapov, and Sergey Simakin who assisted with microprobe analysis.

Conflicts of Interest: The authors declare no conflicts of interest.

References

1. Hensen, B.J.; Zhou, B.; Thost, D.E. Are reaction textures reliable guides to metamorphic histories? Timing constraints from Sm-Nd chronology for "decompression" textures in granulites from Søstrene Island, Prydz Bay, Antarctica. *Geol. J.* **1995**, *30*, 261–271. [CrossRef]
2. Gibson, R.L.; Wallmach, T. Low pressure-high temperature metamorphism in the Vredefort Dome, South Africa: Anticlockwise pressure-temperature path followed by rapid decompression. *Geol. J.* **1995**, *30*, 319–331. [CrossRef]
3. Jöns, N.; Schenk, V.; Appel, P.; Razakamanana, T. Two-stage metamorphic evolution of the Bemarivo Belt of northern Madagascar: Constraints from reaction textures and in situ monazite dating. *J. Metamorph. Geol.* **2006**, *24*, 329–347. [CrossRef]
4. Wiederkehr, M.; Bousquet, R.; Schmid, S.M.; Berger, A. From subduction to collision: Thermal overprint of HP/LT meta-sediments in the north-eastern Lepontine Dome (Swiss Alps) and consequences regarding the tectono-metamorphic evolution of the Alpine orogenic wedge. *Swiss J. Geosci.* **2008**, *101*, 127–155. [CrossRef]
5. Jeřábek, P.; Konopásek, J.; Žáčková, E. Two-stage exhumation of subducted Saxothuringian continental crust records underplating in the subduction channel and collisional forced folding (Krkonoše-Jizera Mts., Bohemian Massif). *J. Struct. Geol.* **2016**, *89*, 214–229. [CrossRef]
6. Liao, X.; Liu, L.; Wang, Y.; Cao, Y.; Chen, D.; Dong, Y. Multi-stage metamorphic evolution of retrograde eclogite with a granulite-facies overprint in the Zhaigen area of the North Qinling Belt, China. *Gondwana Res.* **2016**, *30*, 79–96. [CrossRef]
7. Zhou, G.; Zhang, J.; Li, Y.; Lu, Z.; Mao, X.; Teng, X. Metamorphic evolution and tectonic implications of the granulitized eclogites from the Luliangshan Terrane in the North Qaidam Ultrahigh Pressure Metamorphic Belt, NW China: New constraints from phase equilibrium modeling. *J. Earth Sci.* **2019**, *30*, 585–602. [CrossRef]
8. Dwivedi, S.B.; Theunuo, K.; Kumar, R.R. Characterization and metamorphic evolution of Mesoproterozoic granulites from Sonapahar (Meghalaya), NE India, using EPMA monazite dating. *Geol. Mag.* **2020**, *157*, 1409–1427. [CrossRef]
9. Huang, P.; Wei, C.; Dong, J.; Zhang, J. Two-stage exhumation of high-P rocks from the Yuli Belt, Eastern Taiwan: Insights from the metamorphic evolution in subduction channels. *Lithos* **2023**, *440–441*, 107056. [CrossRef]
10. Sheraton, J.W.; Tingey, R.J.; Black, L.P.; Oliver, R.L. Geology of the Bunger Hills area, Antarctica: Implications for Gondwana correlations. *Antarct. Sci.* **1993**, *5*, 85–102. [CrossRef]
11. Clark, D.J.; Hensen, B.J.; Kinny, P.D. Geochronological constraints for a two-stage history of the Albany-Fraser Orogen, Western Australia. *Precambrian Res.* **2000**, *102*, 155–183. [CrossRef]
12. Morrissey, L.J.; Hand, M.; David, E.; Kelsey, D.E. Curious case of agreement between conventional thermobarometry and phase equilibria modelling in granulites: New constraints on P-T estimates in the Antarctica segment of the Musgrave-Albany-Fraser-Wilkes Orogen. *J. Metamorph. Geol.* **2017**, *35*, 1023–1050. [CrossRef]
13. Smits, R.G.; Collins, W.J.; Hand, M.; Dutch, R.; Payne, J. A Proterozoic Wilson cycle identified by Hf isotopes in central Australia: Implications for the assembly of Proterozoic Australia and Rodinia. *Geology* **2014**, *42*, 231–234. [CrossRef]
14. Aitken, A.R.A.; Betts, P.G.; Young, D.A.; Blankenship, D.D.; Roberts, J.L.; Siegert, M.J. The Australo-Antarctic Columbia to Gondwana transition. *Gondwana Res.* **2015**, *29*, 136–152. [CrossRef]
15. Tucker, N.M.; Payne, J.L.; Clark, C.; Hand, M.; Taylor, R.J.M.; Kylander-Clark, A.R.C.; Martin, L. Proterozoic reworking of Archean (Yilgarn) basement in the Bunger Hills, East Antarctica. *Precambrian Res.* **2017**, *298*, 16–38. [CrossRef]
16. Sheraton, J.W.; Black, L.P.; Tindle, A.G. Petrogenesis of plutonic rocks in a Proterozoic granulite-facies terrane—The Bunger Hills, East Antarctica. *Chem. Geol.* **1992**, *97*, 163–198. [CrossRef]
17. Tucker, N.M.; Hand, M.; Kelsey, D.E.; Taylor, R.; Clark, C.; Paynee, J.L. A tripartite approach to unearthing the duration of high temperature conditions versus peak metamorphism: An example from the Bunger Hills, East Antarctica. *Precambrian Res.* **2018**, *314*, 194–220. [CrossRef]
18. Abdrakhmanov, I.A.; Gulbin, Y.L.; Gembitskaya, I.M. Fe-Mg-Al-Ti-Zn oxide assemblage in granulites of the Bunger Hills, East Antarctica: Evidence of ultrahigh-temperature metamorphism. *Zapiski RMO (Proc. Russian Miner. Soc.)* **2021**, *150*, 38–76. (In Russian)English translation *Geol. Ore Depos.* **2022**, *64*, 519–549 [CrossRef]
19. Gulbin, Y.L.; Abdrakhmanov, I.A.; Gembitskaya, I.M.; Vasiliev, E.A. Oriented micro-inclusions of Al-Fe-Mg-Ti oxides in quartz from metapelitic granulites of the Bunger Hills, East Antarctica. *Zapiski RMO (Proc. Russian Miner. Soc.)* **2022**, *151*, 1–17. (In Russian)English translation *Geol. Ore Depos.* **2023**, *65*, 656–668.
20. Stüwe, K.; Powell, R. Metamorphic evolution of the Bunger Hills, East Antarctica: Evidence for substantial post-metamorphic peak compression with minimal cooling in a Proterozoic orogenic event. *J. Metamorph. Geol.* **1989**, *7*, 449–464. [CrossRef]
21. Harley, S.L. The origins of granulites: A metamorphic perspective. *Geol. Mag.* **1989**, *126*, 215–247. [CrossRef]
22. Collins, W.J. Nature of extensional accretionary orogens. *Tectonics* **2002**, *21*, 1024. [CrossRef]
23. Collins, W.J. Hot orogens, tectonic switching, and creation of continental crust. *Geology* **2002**, *30*, 535–538. [CrossRef]
24. Brown, M. Metamorphic conditions in orogenic belts: A record of secular change. *Int. Geol. Rev.* **2007**, *49*, 193–234. [CrossRef]
25. Kelsey, D.E.; Hand, M. On ultrahigh temperature crustal metamorphism: Phase equilibria, trace element thermometry, bulk composition, heat sources, timescales and tectonic settings. *Geosci. Front.* **2015**, *6*, 311–356. [CrossRef]
26. Tucker, N.M.; Hand, M. New constraints on metamorphism in the Highjump Archipelago, East Antarctica. *Antarct. Sci.* **2016**, *28*, 487–503. [CrossRef]
27. Voronov, P.S. On the structure of Antarctica. *Proc. Inst. Geol. Arctic.* **1960**, *113*, 5–24. (In Russian)

28. Ravich, M.G.; Klimov, L.V.; Solov'ev, D.S. *The Pre-Cambrian of East Antarctica*; Israel Program for Scientific Translations: Jerusalem, Israel, 1968.
29. Stüwe, K.; Wilson, C.J.L. Interaction between deformation and charnockite emplacement in the Bunger Hills, East Antarctica. *J. Struct. Geol.* **1990**, *12*, 767–783. [CrossRef]
30. Sheraton, J.W.; Tingey, R.J.; Oliver, R.L.; Black, L.P. Geology of the Bunger Hills-Denman Glacier region, East Antarctic. *AGSO Bull.* **1995**, *244*, 1–136.
31. Smirnov, V.K.; Sobolev, A.V.; Batanova, V.G.; Portnyagin, M.V.; Simakin, S.G.; Potapov, E.V. Quantitative SIMS analysis of melt inclusions and host minerals for trace elements and H_2O. *Eos Trans. Spring Meet. Suppl. AGU* **1995**, *76*, 270.
32. Nosova, A.A.; Narkisova, V.V.; Sazonova, L.V.; Simakin, S.G. Minor elements in clinopyroxene from Paleozoic volcanics of the Tagil island arc in the Central Urals. *Geochem. Int.* **2002**, *40*, 219–232.
33. McDonough, W.F.; Sun, S.S. The composition of the Earth. *Chem. Geol.* **1995**, *120*, 223–253. [CrossRef]
34. Harley, S.L.; Green, D.H. Garnet-orthopyroxene barometry for granulites and peridotites. *Nature* **1982**, *300*, 697–701. [CrossRef]
35. Lee, H.Y.; Ganguly, J. Equilibrium compositions of coexisting garnet and orthopyroxene: Experimental determinations in the system FeO-MgO-Al_2O_3-SiO_2, and applications. *J. Petrol.* **1988**, *29*, 93–113. [CrossRef]
36. Thomas, J.; Watson, E.B.; Spear, F.S.; Shemella, P.T.; Nayak, S.K.; Lanzirotti, A. TitaniQ under pressure: The effect of pressure and temperature on the solubility of Ti in quartz. *Contrib. Mineral. Petrol.* **2010**, *160*, 743–759. [CrossRef]
37. Huang, R.; Audétat, A. The titanium-in-quartz (TitaniQ) thermobarometer: A critical examination and re-calibration. *Geochim. Cosmochim. Acta* **2012**, *84*, 75–89. [CrossRef]
38. Henry, D.J.; Guidotti, C.V.; Thomson, J.A. The Ti-saturation surface for low-to-medium pressure metapelitic biotites: Implications for geothermometry and Ti-substitution mechanisms. *Am. Mineral.* **2005**, *90*, 316–328. [CrossRef]
39. Hokada, T. Feldspar thermometry in ultrahigh-temperature metamorphic rocks: Evidence of crustal metamorphism attaining ~1100 °C in the Archean Napier Complex, East Antarctica. *Am. Mineral.* **2001**, *86*, 932–938. [CrossRef]
40. Fuhrman, M.L.; Lindsley, D.H. Ternary-feldspar modeling and thermometry. *Am. Mineral.* **1988**, *73*, 201–215.
41. Reche, J.; Martinez, F.J. GPT: An excel spreadsheet for thermobarometric calculations in metapelitic rocks. *Comp. Geosci.* **1996**, *22*, 775–784. [CrossRef]
42. De Capitani, C.; Petrakakis, K. The computation of equilibrium assemblage diagrams with Theriak/Domino software. *Am. Mineral.* **2010**, *95*, 1006–1016. [CrossRef]
43. Holland, T.J.B.; Powell, R. An internally consistent thermodynamic data set for phases of petrological interest. *J. Metamorph. Geol.* **1998**, *16*, 309–343. [CrossRef]
44. Baldwin, J.A.; Powell, R.; Brown, M.; Moraes, R.; Fuck, R.A. Modelling of mineral equilibria in ultrahigh temperature metamorphic rocks from the Anapolis–Itaucu Complex, central Brazil. *J. Metamorph. Geol.* **2005**, *23*, 511–523. [CrossRef]
45. White, R.W.; Powell, R.; Clarke, G.L. The interpretation of reaction textures in Fe-rich metapelitic granulites of the Musgrave Block, central Australia: Constraints from mineral equilibria calculations in the system K_2O–FeO–MgO–Al_2O_3–SiO_2–H_2O–TiO_2–Fe_2O_3. *J. Metamorph. Geol.* **2002**, *20*, 41–55. [CrossRef]
46. White, R.W.; Powell, R.; Holland, T.J.B. Progress relating to calculation of partial melting equilibria for metapelites. *J. Metamorph. Geol.* **2007**, *25*, 511–527. [CrossRef]
47. Kelsey, D.E.; White, R.W.; Holland, T.J.B.; Powell, R. Calculated phase equilibria in K_2O-FeO-MgO-Al_2O_3-SiO_2-H_2O for sapphirine-quartz-bearing mineral assemblages. *J. Metamorph. Geol.* **2004**, *22*, 559–578. [CrossRef]
48. Whitney, D.L.; Evans, B.W. Abbreviations for names of rock-forming minerals. *Am. Mineral.* **2010**, *95*, 185–187. [CrossRef]
49. Holness, M.B.; Cesare, B.; Sawyer, E.W. Melted rocks under the microscope: Microstructures and their interpretation. *Elements* **2011**, *7*, 247–252. [CrossRef]
50. Harley, S.L.; Kelly, N.M. The impact of zircon-garnet REE distribution data on the interpretation of zircon U-Pb ages in complex high-grade terrains: An example from the Rauer Islands, East Antarctica. *Chem. Geol.* **2007**, *241*, 62–87. [CrossRef]
51. Harley, S.L. Refining the P-T records of UHT crustal metamorphism. *J. Metamorph. Geol.* **2008**, *26*, 125–154. [CrossRef]
52. Kelsey, D.E. On ultrahigh-temperature crustal metamorphism. *Gondwana Res.* **2008**, *13*, 1–29. [CrossRef]
53. Harley, S.L. Garnet-orthopyroxene bearing granulites from Enderby Land, Antarctica: Metamorphic pressure-temperature-time evolution of the Archaean Napier Complex. *J. Petrol.* **1985**, *26*, 819–856. [CrossRef]
54. McFarlane, C.R.M.; Carlson, W.D.; Connely, J.N. Prograde, peak, and retrograde P-T paths from aluminium in orthopyroxene: High-temperature contact metamorphism in the aureole of the Makhavinekh Lake Pluton, Nain Plutonic Suite, Labrador. *J. Metamorph. Geol.* **2003**, *21*, 405–423. [CrossRef]
55. Brandt, S.; Klemd, R.; Okrusch, M. Ultrahigh-temperature metamorphism and multistage evolution of garnet-orthopyroxene granulites from the Proterozoic Epupa Complex, NW Namibia. *J. Petrol.* **2003**, *44*, 1121–1144. [CrossRef]
56. Tsunogae, T.; Miyano, T.; van Reenen, D.D.; Smit, C.A. Ultrahigh-temperature metamorphism of the Southern Marginal Zone of the Archean Limpopo Belt, South Africa. *J. Mineral. Petrol. Sci.* **2004**, *99*, 213–224. [CrossRef]
57. Ishii, S.; Tsunogae, T.; Santosh, M. Ultrahigh-temperature metamorphism in the Achankovil Zone: Implications for the correlation of crustal blocks in southern India. *Gondwana Res.* **2006**, *10*, 99–114. [CrossRef]
58. Tadokoro, H.; Tsunogae, T.; Santosh, M.; Yoshimura, Y. First report of the spinel + quartz assemblage from Kodaikanal in the Madurai Block, Southern India: Implications for ultrahigh-temperature metamorphism. *Int. Geol. Rev.* **2007**, *49*, 1050–1068. [CrossRef]

59. Santosh, M.; Tsunogae, T.; Li, J.H.; Liu, S.J. Discovery of sapphirine-bearing Mg-Al granulites in the North China Craton: Implications for Paleoproterozoic ultrahigh-temperature metamorphism. *Gondwana Res.* **2007**, *11*, 263–285. [CrossRef]
60. Bhandari, A.; Pant, N.C.; Bhowmick, S.K.; Goswami, S. 1.6 Ga ultrahigh-temperature granulite metamorphism in the Central Indian Tectonic Zone: Insights from metamorphic reaction history, geothermobarometry and monazite chemical ages. *Geol. J.* **2011**, *46*, 198–216. [CrossRef]
61. Sukhorukov, V.P.; Turkina, O.M.; Tessalina, S.; Talavera, C. Sapphirine-bearing Fe-rich granulites in the SW Siberian craton (Angara-Kan block): Implications for Paleoproterozoic ultrahigh-temperature metamorphism. *Gondwana Res.* **2018**, *57*, 26–47. [CrossRef]
62. Pattison, D.R.M.; Chacko, T.; Farquhar, J.; McFarlane, C.R.M. Temperatures of granulite-facies metamorphism: Constraints from experimental phase equilibria and thermobarometry corrected for retrograde exchange. *J. Petrol.* **2003**, *44*, 867–900. [CrossRef]
63. Hensen, B.J.; Harley, S.L. Graphical analysis of P-T-X relations in granulite facies metapelite. In *High-Temperature Metamorphism and Crustal Anataxis*; Ashworth, J.R., Brown, M., Eds.; Unwin Hyman: London, UK, 1990; pp. 19–56.
64. Tateishi, K.; Tsunogae, T.; Santosh, M.; Janardhan, A.S. First report of sapphirine +quartz assemblage from Southern India: Implications for ultrahigh-temperature metamorphism. *Gondwana Res.* **2004**, *7*, 899–912. [CrossRef]
65. Pilugin, S.M.; Fonarev, V.I.; Savko, K.A. Feldspar thermometry of ultrahigh-temperature ($\geq$ 1000 °C) metapelites from the Voronezh Crystalline Massif (Kursk-Besedino Granulite Block). *Dokl. Earth Sci.* **2009**, *425*, 201–204. [CrossRef]
66. Martignole, J.; Wang, Z. Feldspar thermometry of Grenvillian-age UHT migmatites, Mollendo-Camana block, southern Peru. *Can. Mineral.* **2010**, *48*, 1025–1039. [CrossRef]
67. Jiao, S.; Guo, J. Application of the two-feldspar geothermometer to ultrahigh-temperature (UHT) rocks in the Khondalite belt, North China craton and its implications. *Am. Mineral.* **2011**, *96*, 250–260. [CrossRef]
68. Nanne, J.A.M.; de Roever, E.W.F.; de Groot, K.; Davies, G.R.; Brouwer, F.M. Regional UHT metamorphism with widespread, primary CO2-rich cordierite in the Bakhuis Granulite Belt, Surinam: A feldspar thermometry study. *Precambrian Res.* **2020**, *350*, 105894. [CrossRef]
69. Elkins, L.T.; Grove, T.L. Ternary feldspars experiments and thermodynamic models. *Am. Mineral.* **1990**, *75*, 544–559.
70. Yavuz, F.; Yavuz, E.V. A Windows program for feldspar group thermometers and hygrometers. *Period. Mineral.* **2022**, *91*, 63–87. [CrossRef] [PubMed]
71. Cherniak, D.J.; Watson, E.B.; Wark, D.A. Ti diffusion in quartz. *Chem. Geol.* **2007**, *236*, 65–74. [CrossRef]
72. Sato, K.; Santosh, M. Titanium in quartz as a record of ultrahigh-temperature metamorphism: The granulites of Karur, southern India. *Miner. Mag* **2007**, *71*, 143–154. [CrossRef]
73. Adachi, T.; Hokada, T.; Osanai, Y.; Toyoshima, T.; Baba, S.; Nakano, N. Titanium behavior in quartz during retrograde hydration: Occurrence of rutile exsolution and implications for metamorphic processes in the Sør Rondane Mountains, East Antarctica. *Polar Sci.* **2010**, *3*, 222–234. [CrossRef]
74. Ewing, T.A.; Hermann, J.; Rubatto, D. The robustness of the Zr-in-rutile and Ti-in-zircon thermometers during high-temperature metamorphism (Ivreae-Verbano Zone, northern Italy). *Contrib. Mineral. Petrol.* **2013**, *165*, 757–779. [CrossRef]
75. Buddington, A.F.; Lindsley, D.H. Iron-titanium oxide minerals and synthetic equivalents. *J. Petrol.* **1964**, *5*, 310–357. [CrossRef]
76. Bohlen, S.R.; Essene, E.J. Feldspar and oxide thermometry of granulites in the Adirondack Highlands. *Contrib. Mineral. Petrol.* **1977**, *62*, 153–169. [CrossRef]
77. Rollinson, H.R. Iron-titanium oxides as an indicator of the role of the fluid phase during the cooling of granites metamorphosed to granulite grade. *Mineral. Mag.* **1980**, *43*, 623–631. [CrossRef]
78. Harlov, D.E. Titaniferous magnetite-ilmenite thermometry and titaniferous magnetite-ilmenite-orthopyroxene-quartz oxygen barometry in granulite facies gneisses, Bamble Sector, SE Norway: Implications for the role of high-grade CO_2-rich fluids during granulite genesis. *Contrib. Mineral. Petrol.* **2000**, *139*, 180–197. [CrossRef]
79. Oliver, G.J.H. Ilmenite-magnetite geothermometry and oxygen barometry in granulite and amphibolite facies gneisses from Doubtful Sound, Fiordland, New Zealand. *Lithos.* **1978**, *11*, 147–153. [CrossRef]
80. Andersen, D.J.; Lindsley, D.H. New (and final!) models for the Ti-magnetite/ilmenite geothermometer and oxygen barometer. *Abstract AGU 1985 Spring Meeting Eos Transactions. American Geophysical Union.* **1985**, *66*, 416.
81. Sauerzapf, U.; Lattard, D..; Burchard, M.; Engelmann, R. The titanomagnetite-ilmenite equilibrium: New experimental data and thermo-oxybarometric application to the crystallization of basic to intermediate rocks. *J. Petrol.* **2008**, *49*, 1161–1185. [CrossRef]
82. Nichols, G.T.; Berry, R.F.; Green, D.H. Internally consistent gahnitic spinel-cordierite-garnet equilibria in the FMASHZn system: Geothermobarometry and applications. *Contrib. Mineral. Petrol.* **1992**, *111*, 362–377. [CrossRef]
83. Clarke, G.L.; Powell, R.; Guiraud, M. Low-pressure granulite facies metapelitic assemblages and corona textures from MacRobertson land, east Antarctica: The importance of Fe_2O_3 and TiO_2 in accounting for spinel-bearing assemblages. *J. Metamorph. Geol.* **1989**, *7*, 323–335. [CrossRef]
84. Boger, S.D.; White, R.W. The metamorphic evolution of metapelitic granulites from Radok Lake, northern Prince Charles Mountains, east Antarctica; evidence for an anticlockwise P–T path. *J. Metamorph. Geol.* **2003**, *21*, 285–298. [CrossRef]
85. Halpin, J.A.; White, R.W.; Clarke, G.K.; Kelsey, D.E. The Proterozoic P-T-t evolution of the Kemp Land Coast, East Antarctica; Constraints from Si-saturated and Si-undersaturated metapelites. *J. Petrol.* **2007**, *48*, 1321–1349. [CrossRef]
86. Vernon, R.H. Formation of late sillimanite by hydrogen metasomatism (base-leaching) in some high-grade gneisses. *Lithos* **1989**, *12*, 143–152. [CrossRef]

87. Bohlen, S.R. Pressure-temperature-time paths and a tectonic model for the evolution of granulites. *J. Geol.* **1987**, *95*, 617–632. [CrossRef]
88. England, P.C.; Thompson, A.B. Pressure–temperature–time paths of regional metamorphism I. *Heat transfer during the evolution of regions of thickened continental crust. J. Petrol.* **1984**, *25*, 894–928.
89. Wells, P.R.A. Thermal models for the magmatic accretion and subsequent metamorphism of continental crust. *Earth Planet. Sci. Lett.* **1980**, *46*, 253–265. [CrossRef]
90. Sandiford, M.; Powell, R. Deep crustal metamorphism during continental extension: Modern and ancient examples. *Earth Planet. Sci. Lett.* **1986**, *79*, 151–158. [CrossRef]
91. Myers, J.S. Precambrian tectonic evolution of part of Gondwana, southwestern Australia. *Geology* **1990**, *18*, 537–540. [CrossRef]
92. Clark, C.; Kirkland, C.L.; Spaggiari, C.V.; Oorschot, C.; Wingate, M.T.D.; Taylor, R.J. Proterozoic granulite formation driven by mafic magmatism: An example from the Fraser Range Metamorphics, Western Australia. *Precambrian Res.* **2014**, *240*, 1–21.
93. Spaggiari, C.V.; Kirkland, C.L.; Smithies, R.H.; Wingate, M.T.D.; Belousova, E.A. Transformation of an Archean craton margin during Proterozoic basin formation and magmatism: The Albany–Fraser Orogen, Western Australia. *Precambrian Res.* **2015**, *266*, 440–466. [CrossRef]
94. Smithies, R.H.; Howard, H.M.; Evins, P.M.; Kirkland, C.L.; Kelsey, D.E.; Hand, M.; Wingate, M.T.D.; Collins, A.S.; Belousova, E. High-temperature granite magmatism, crust-mantle interaction and the Mesoproterozoic intracontinental evolution of the Musgrave Province, Central Australia. *J. Petrol.* **2011**, *52*, 931–958. [CrossRef]